LASER & PHOTONICS REVIEWS

www.lpr-journal.org

Rejuvenating a Versatile Photonic Material: Thin-Film Lithium Niobate

*Amirmahdi Honardoost, Kamal Abdelsalam, and Sasan Fathpour **

The excellent optical and unique material properties of lithium niobate have long established it as a prevailing photonic material, especially for the long-haul telecom modulator and wavelength-converter applications. However, conventional lithium niobate optical waveguides are bulky, hence large-scale photonic circuit implementations are impeded and high power requirements are imposed. To address these shortcomings, thin-film lithium niobate technology has been a topic of intense research in the last few years and a plethora of ultracompact devices with significantly superior performances than the conventional counterparts have been demonstrated. These efforts have rejuvenated lithium niobate for novel electro-, nonlinear-, and quantum-optic applications. Herein, the most recent advancements of this booming field are summarized and a perspective for future directions is given.

1. Introduction

Lithium niobate ($LiNbO_3$, LN) has been recognized as a versatile material for over half a century, thanks to its strong ferroelectric, piezoelectric, electrooptic, thermooptic, acoustooptic, pyroelectric and other properties.[1] Improvements in bulk crystal growth by the Czochralski technique has rendered LN a dominant choice for applications based on these properties, as summarized in **Figure 1**a. Particularly for optical applications, strong electrooptic (EO) coefficient ($r_{33} \approx 31$ pm V^{-1} at 633-nm wavelength), large nonlinearity ($d_{33} = 27$ pm V^{-1} at 1064-nm wavelength), remarkable thermooptic birefringence and a broad transparency range in the electromagnetic spectrum (~0.35 – 5 μm) ought to be highlighted.[2–6] Indeed, LN has been the standard material of choice for the EO modulators used in long-haul communication[7] and nonlinear wavelength-converters.[8] Several commercial off-the-shelf modulator products are available with high performance, that is, up to 50 GHz bandwidth (BW) and large extinction ratios (ER).[9–11] Also, ~250 %W^{-1}cm^{-2} normalized conversion efficiency for second-harmonic generation (SHG) has been commercialized.[12–14]

With the ever-increasing complexity of modern optical systems, there has been a growing demand for reduction in power consumption, device footprint, and manufacturing cost of photonic integrated circuits (PICs) in the past decades. While the mature silicon (Si) photonic technology can meet these requirements,[15–18] owing to its standard low-cost foundry-compatible processing and tightly-confined waveguides, the performance of LN-based modulators and wavelength converters are unrivaled by their all-Si-based counterparts. Lack of linear EO via Pockel's effect, lack of second-order nonlinearity ($\chi^{(2)}$) due to silicon's centrosymmetric lattice structure, and nonlinear two-photon and free-carrier absorption effects are among the hurdles of silicon photonics.[4]

On the other hand, conventional LN devices are bulky and power hungry in general. Traditionally, LN waveguides are commonly formed by in-diffusion of dopants, such as titanium (Ti),[19] or proton-exchange (PE)[20] processes. While low propagation loss is attainable, these methods only slightly alter the refractive index of the material ($\Delta n \approx 0.1$), which yields in weak optical confinement. Hence, conventional LN devices suffer from a number of shortcomings, including large bending radii in general, increased half-wave voltage-length product ($V_\pi \cdot L$), and long Mach–Zehnder (MZ) arm lengths for EO modulators,[21,22] as well as limited nonlinear conversion efficiency due to the inefficient overlap of the resultant large optical modes in guided devices for wavelength conversion, for example, periodically poled LN (PPLN) waveguides for SHG.[8,23] Essentially, these shortcomings impede the exploitation of conventional bulk LN devices for large-scale PICs.

As a solution, thin-film LN (TFLN) approaches have been pursued since 2004[30] by using crystal ion slicing[31] and room-temperature wafer bonding[32,33] methods. TFLN on Si substrate was first demonstrated at CREOL in 2013.[29] Among other advantages (e.g., cost, scalability, ease of handling thermal cycles), the choice of Si substrate has paved the path toward heterogeneous integration of TFLN devices with Si photonics. Since

Dr. A. Honardoost, [+] K. Abdelsalam, Prof. S. Fathpour
CREOL
The College of Optics and Photonics
University of Central Florida
Orlando FL 32816, USA
E-mail: fathpour@creol.ucf.edu
Dr. A. Honardoost, Prof. S. Fathpour
Department of Electrical and Computer Engineering
University of Central Florida
Orlando, FL 32816, USA

[+]Present address: Department of Electrical Engineering and Computer Sciences, University of California, Berkeley, CA 94720, USA

DOI: 10.1002/lpor.202000088

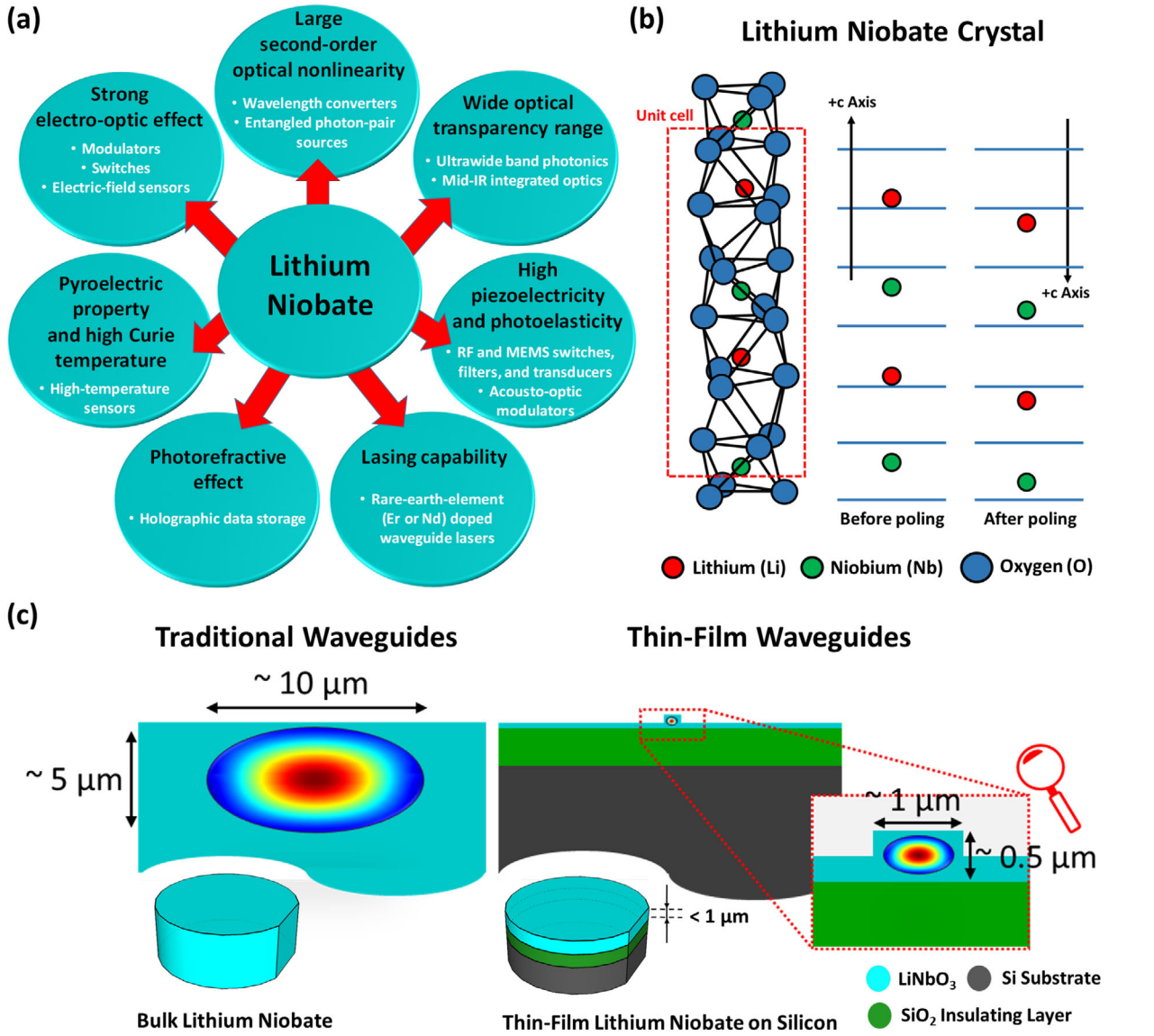

Figure 1. a) Summary of unique material properties of LN.[1–8,24–27] This review focuses on the main photonic applications of LN through exploiting its strong EO effect and large second-order optical nonlinearity; b) Crystalline structure of LN in ferroelectric phase. The red dashed-box represents its unit cell. The horizontal blue lines depict the oxygen (O) layers and the position of lithium (Li) and niobium (Nb) atoms are shown with respect to it (after ref. [2, 28]). The position of the atoms are shown before and after the poling process, as discussed in Section 4.1; c) Comparison between the traditional bulk versus thin-film LN waveguides. The figures for the waveguides cross-sections are drawn to scale to emphasize the significant reduction in optical mode size. This about two orders of magnitude reduction facilitates large-scale integration of photonic integrated circuits, as well as boosted performance for LN devices, for example, reduced $V_\pi \cdot L$ for TFLN EOMs and increased mode overlap and efficiency for PPLN waveguides. The steps for fabrication of TFLN wafers on Si are presented in Figure 2.

then, commercialization of TFLN wafers by a CREOL spinoff company,[34] as well as other vendors,[35,36] have facilitated the availability of this platform for extensive research. In addition, other methods such as direct bonding[37] and benzocyclobutene (BCB) bonding[38] of individual TFLN dies on Si, as well as mechanical thinning of bulk LN,[39] have been pursued. In order to achieve low-loss submicron waveguides, several methods have been demonstrated on the TFLN technology. They include rib-loading with a refractive-index-matched material,[29,40–44] dry etching,[45–50] ion-beam-enhanced etching,[51] PE,[52,53] Ti in-diffusion,[54] direct- or BCB-bonding on silicon-on-insulator (SOI),[38,55,56] plasma-enhanced chemical deposition (PECVD) of other materials, such as amorphous Si,[57] optical-grade dicing,[58] and mechanical thinning.[39] The optical mode size in these waveguides is typically reduced by about two orders of magnitude compared to their bulk counterparts (see Figure 1c).

In recent years, based on this rapidly-growing technology, a plethora of ultracompact integrated photonic devices and circuits, such as microdisk[59–62] and microring[46,63–66] resonators, EO modulators,[67–85] acousto-optic modulators,[86–89] photodetector,[90] integrated single-photon detector,[91] grating couplers,[92–96] fiber-to-chip edge couplers,[97–99] wavelength

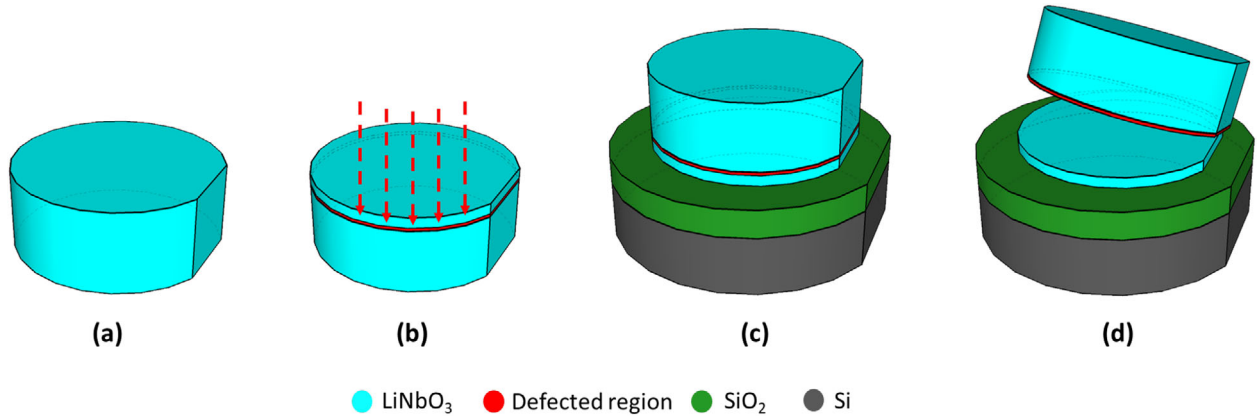

Figure 2. Summary of the steps for fabrication of TFLN on Si wafers.[29] a) Initial bulk LN wafer; b) Ion implantation (the red-dashed line shows the defected region at the desired depth of final thin-film thickness); c) Bonding onto a Si handling wafer (or other wafers such as LN or quartz) with a low-index insulating layer (typically SiO_2); d) Thermal cycling process to exfoliate the thin film from the LN crystal at the defected layer and the final TFLN on Si product. The remaining bulk LN crystal can be recycled. For simplicity, other steps such as thermal annealing for preserving the material properties of LN, and mechanical polishing for smoothening of the surface roughness are not depicted here.

converters,[100–111] and entangled-photon sources[112–116] with significantly superior performances than their conventional LN counterparts have been demonstrated. The overall efforts have rejuvenated LN for novel electro-, nonlinear-, and quantum-optic applications and the material is considered among the top candidates for heterogeneous integrated photonics, where multiple materials are monolithically integrated on a single chip, while each material is chosen for the functionalities that suits it best.

Here, we summarize the most recent advancements of this flourishing field for its main photonic applications. The review is structured as follows. Section 2 gives a brief overview of the strides made toward the realization of ultracompact TFLN waveguides with the mentioned various approaches and the associated challenges in order to achieve low-propagation loss. In Sections 3–5 the path from first realization to the state-of-the-art performance is chronologically reviewed for electro-, nonlinear-, and quantum-optic applications, respectively. Section 6 lays out a roadmap for future directions, and concluding remarks are given in Section 7.

For completeness, it should be mentioned that the detailed design guidelines of these devices are obviously beyond the scope of this work. Moreover, it is noted that while this paper focuses on various advancements of TFLN field, realization of ultracompact integrated photonic devices, such as EO modulators and wavelength converters are not limited to this platform. For other material platforms, readers are referred to relevant references.[117–121]

2. TFLN Platforms and Waveguides

2.1. Thin-Film Platforms

As mentioned in the Introduction, TFLN approaches have been pursued in order to overcome the drawbacks associated with bulk LN devices and have led to the LN-on-insulator (LNOI) platform. The insulator layer is comprised of a lower refractive index material, such as silicon dioxide (SiO_2), in order to avoid optical mode leakage from the thin film into the substrate. Among different choice of substrates, for example, LN and Quartz, Si has been the most attractive one due to its potential for compatibility with Si photonics.[29] As mentioned before, other attributions such as cost, scalability, and thermal handling are important too.

In this approach, single-crystalline LN is implanted with helium (He) or other low-mass ions. Next, the ion-implanted wafer is bonded to an oxidized Si wafer. Then, through thermal cycling processes, the TFLN is exfoliated from the bulk crystal and remains bonded onto the oxidized Si substrate. It has been shown that the EO and nonlinear properties of LN is preserved at the end of the process.[122] **Figure 2** summarizes the fabrication steps for this method. Currently, TFLN wafers on Si and other substrates with different crystal cuts are commercially available from suppliers in the United States,[34] in China,[35] and in Japan.[36]

Another approach is using polymers, such as BCB, for bonding individual dies or full wafers of TFLN to Si.[37,38,63,67] However, thermal stability and temporal reliability of polymers remain a major concern.[4,74,123]

2.2. Ultracompact Waveguides

As summarized in **Figure 3**, various approaches have been pursued in order to form optical waveguides on TFLN. In the following, we discuss these approaches and explore their merits.

Historically, LN has been difficult to etch and the roughness of the etched sidewalls, as well as re-deposition of the chemical-etching byproducts, have contributed to large amounts of scattering and propagation losses.[22,120] As a solution, one method has been to rib-load the TFLN with a material whose its refractive index (~2–2.2) is close to that of LN (~2.2) (see Figure 3a). One of the main advantages of this method is the ease of processing. Several materials have been pursued in this regard, such as tantalum pentoxide (Ta_2O_5),[29] chalcogenide glass (ChG),[70] silicon nitride (SiN, Si_3N_4),[41,71,72,81,85,100,101,124] and titanium dioxide (TiO_2),[40] with reported propagation loss values as low as ~1 dB cm^{-1} for plasma-enhanced chemical-vapor deposition

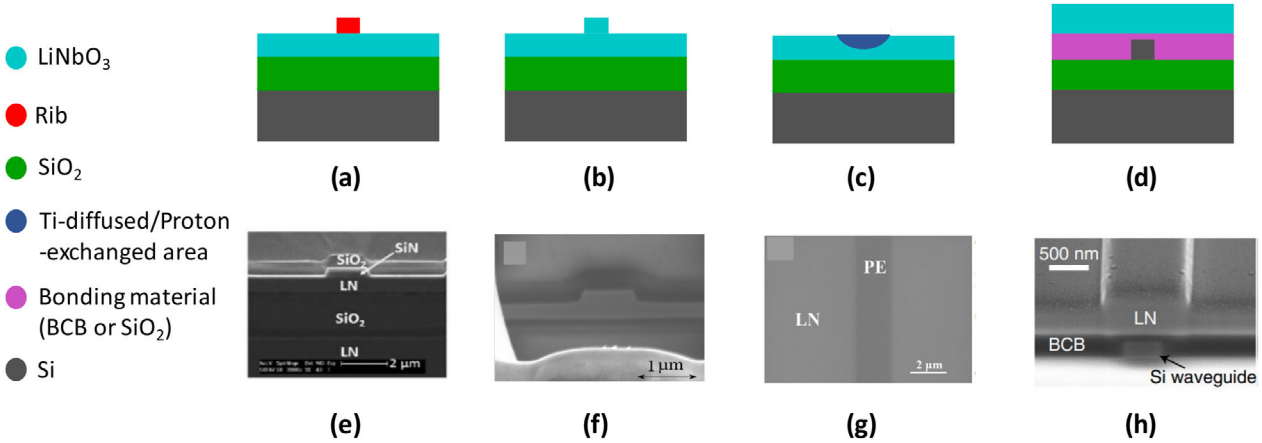

Figure 3. Common waveguide structures for TFLN-on-Si devices: a) Rib-loaded, b) dry-etched, c) proton-exchanged or Ti-diffused, and d) SOI-bonded structures; These methods can also be applied to TFLN on LN or quartz substrates. The majority of recent work demonstrating high-performance TFLN EOMs are utilizing rib-loaded (Figure 3a),[71] dry-etched (Figure 3b),[75,78] and SOI-bonded (Figure 3d)[76,77,80,84] methods, while for nonlinear devices, rib-loaded[100,101] and dry-etched[102,105] have been the most commonly employed platforms. In comparison to platforms (a)–(c), platform (d) requires additional bonding and TFLN substrate removal steps. e) Reproduced with permission.[47] Copyright 2018, The Optical Society. f) Reproduced with permission.[53] Copyright 2015, The Optical Society. g) Reproduced with permission.[101] Copyright 2016, The Optical Society. h) Reproduced with permission.[80] Copyright 2019, Springer Nature.

(PECVD) of SiN rib.[71,100] Although other forms of deposition, such as low-pressure chemical-vapor deposition (LPCVD), can offer rib materials with much lower propagation loss, the standard TFLN wafers cannot withstand the high temperature used in these type of processes. Alternatively, LPCVD-SiN can be bonded to TFLN,[41,43] offering loss values as low as ~0.3 dB cm^{-1}.[41]

The rib material's effective index and dimensions can be engineered to provide high optical mode overlap (more than 70%) in TFLN, in order to efficiently utilize its EO and nonlinear properties.[120] Another advantage of rib-loaded method is that it can be applied to all crystal cuts of TFLN, whereas some other methods which are discussed in the following, can only be applied to certain cuts. This method has also been utilized for bulk LN crystals in order to form compact waveguides using monocrystalline[126,127] or amorphous[57] Si.

More recently, promising works[45–49] have been reported on low-loss dry-etching of LN with reported loss values as low as 0.027 dB cm^{-1}[46] for *X*-cut, and <2-nm sidewall roughness[47] for *Z*-cut TFLN. Following the dry-etching of LN, the waveguides have to undergo a thorough RCA cleaning step in order to remove the organic residue and chemical byproducts of the etching process.[45,49] In a recent work,[48] a combination of PE and dry etching is presented for efficient direct-etching of TFLN, that is, faster etch rates while avoiding re-deposition of byproducts. By using this method, low-loss channel waveguides with large etch depths (~900 nm) and improved verticality of sidewalls are reported in *X*-cut TFLN. It is important to note that the dry-etching method can result differently for various crystal cuts of LN, for example, re-deposition of byproducts from dry etching are different for *Z*-cut compared to the *X*- or *Y*-cut LN.[120]

As depicted in Figure 3b, dry-etched waveguides have been also utilized for TFLN EO modulators (EOMs)[73–75,78] and nonlinear devices.[100–102,105] For EOMs, in comparison with rib-loading, this approach provides higher optical confinement in LN, which can consequently result in smaller electrode gaps in MZ-based devices, hence reducing the EOM's V_π. However, in the presence of certain requirements due to ultrahigh-speed design, the rib-loaded method is more advantageous due to the lower dielectric constant of the rib compared to that of LN.[128]

Figure 3c shows another type of waveguide in the TFLN platform. PE or annealed-PE (PE followed by a high-temperature annealing step in order to recover the LN EO properties) processes are low-cost technologies, which are well-established for conventional bulk LN devices.[7,129] In this process, the lithium ions in the crystal are exchanged with protons from an acid bath. This results in a small increase in the extraordinary refractive index, which can confine the optical mode in the exchanged region. This method has been applied to TFLN[52,53] and waveguide loss values as low as 0.2 dB cm^{-1} have been achieved in *X*-cut TFLN.[53] Although the optical mode sized can be reduced to ~ 0.6 μm^2, the main downsides of this platform are weak optical confinement, and very large bending radii, which are two to three orders of magnitude higher than values in other TFLN platforms. Moreover, since the acid chemically etches the *Y*-cut LN, this process can only be applied to *X*- or *Z*-cut TFLN.[7] More recently, in-diffusion of Ti, another well-established process for conventional EOMs, is also utilized in an LNOI structure, and a TFLN MZ EOM is reported.[54]

In order to exploit benefits of the mature Si photonic industry, an interesting type of platform is recently pursued, in which the TFLN is bonded at the end stages of fabrication onto a patterned SOI wafer.[38,125] Figure 3d depicts such a structure. Common types of bonding are direct-bonding using SiO_2,[76,77,80] or by using an adhesive polymer like BCB.[37,38,67–69] However, direct-bonding is usually preferred due to stability and reliability issues with BCB, as previously pointed out in Section 2.1.

The fabrication steps for this platform are summarized in **Figure 4**.[125] Figure 4a shows the prepared SOI waveguides. To form hybrid waveguides, the width of the Si waveguide is decreased, in order to confine most of the optical mode in the TFLN region. As a result of this Si waveguide narrowing, a disadvantage is the more interaction of optical mode with Si waveguide sidewalls

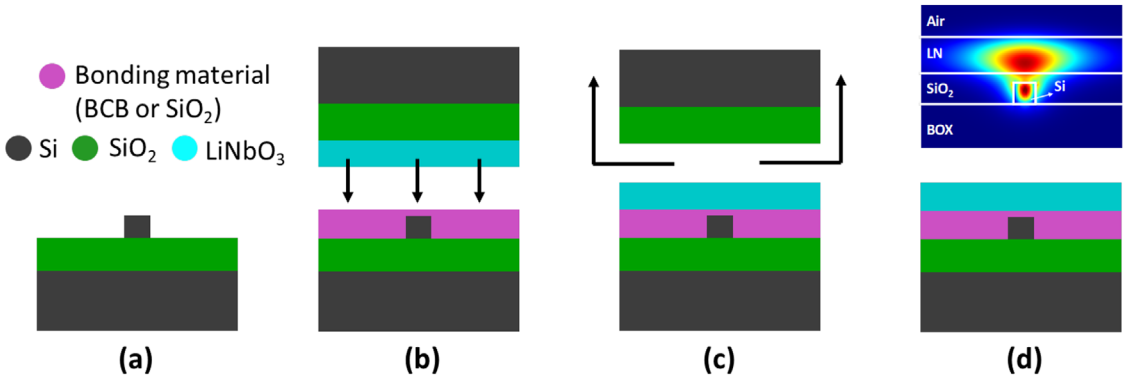

Figure 4. Fabrication steps for bonded-SOI TFLN platform[76,77,80,125]: a) Patterned SOI structure; b) TFLN (see Figure 2d) bonding onto the SOI wafer using SiO_2 or BCB; c) TFLN substrate removal; d) Prepared structure and associated optical mode simulation. At this step, metallic electrodes can be deposited on top in order to form LN photonic devices such as EOM and PPLN waveguides.

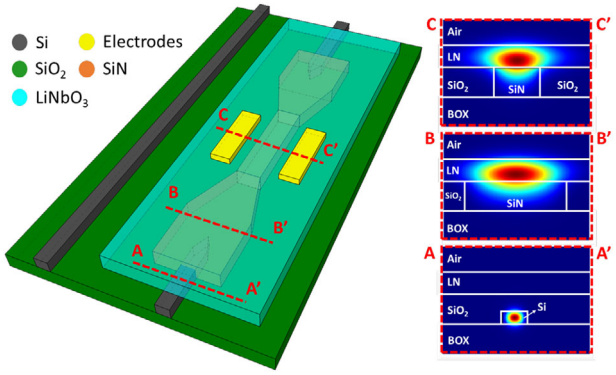

Figure 5. A novel approach for heterogeneous integration of TFLN with SOI waveguides is shown. The SiN intermediate layer serves as the adiabatic mode converter from SOI to the LN region (from *AA'* to *BB'*), as well as the rib for the hybrid SiN-LN waveguide. The optical mode simulation at different cross-sections of the structure are shown on the right. The SiN width can be optimized for achieving the desired optical mode confinement in TFLN.[125]

which could yield in additional loss. Figure 4b,c depicts the TFLN bonding and substrate removal steps, respectively. Another challenge for this approach is achieving the desired amount of thin bonding-material layer between the SOI and TFLN regions. The schematic of the prepared hybrid waveguide and its associate optical mode simulation are shown in Figure 4d. In this step, metallic electrodes can be deposited and patterned on top for realizing EOM or other devices.

A more robust approach is using an intermediate layer, such as LPCVD-formed SiN serving as an adiabatic mode converter as well as a rib, in order to efficiently transfer the optical mode from standard SOI waveguides into LN region[125] (see **Figure 5**). Another variation is to embed the metallic electrodes into the bottom optical waveguide structure, as recently reported for TFLN EOMs[85]. This eliminates the need for TFLN substrate removal and results in a more straightforward fabrication process.

In summary, by employing TFLN technology (see Figure 2d), various methods discussed in this section have resulted in ultracompact TFLN waveguides. The optical mode size and the waveguide propagation loss have been reduced by one to two orders (depending on the waveguide platform choice), and one order of magnitude, respectively, compared to the Ti-diffused or PE bulk LN counterparts.[23,46] The propagation loss values of each TFLN platform are summarized in **Table 1**.

Table 1. State of the art in propagation loss for various TFLN platforms of Figure 3.

TFLN platform	Waveguide loss [dB cm^{-1}]	Reference
Rib-loaded	0.3	[101]
Dry-etched	0.027	[46]
Proton-exchanged	0.2	[53]
SOI-bonded	0.3	[50]

It is noted that among the above mentioned structures, most of the recently-demonstrated high-performance TFLN EOMs have utilized rib-loaded,[71] dry-etched,[75,78] and SOI-bonded[76,80] methods integrated on Si substrate. For nonlinear LN devices, rib-loaded[100,101] and dry-etched[102,105] methods have been employed so far.

3. Electrooptic Modulators on TFLN

There is a host of different applications for high-performance EO-based devices on the TFLN platform. These include optical electric-field sensors,[130] analog and digital optical links for telecommunication systems,[131] and optical interconnects[132] in high-capacity data centers, EO-based frequency comb generation[109,133] for LiDAR, integrated spectroscopy,[134,135] millimeter-wave imaging,[136] and high-performance computing for optical neural networks,[137] as well as quantum technologies.[138] Some applications in visible-wavelength photonics include molecular spectroscopy and biophotonics.[139,140]

In this section, we provide a brief chronological review of the recent advancements for TFLN EOMs. **Figure 6** summarizes the main achievements in terms of key performance parameters, that is, propagation loss, BW, and ER. The comparison between the conventional and ultracompact LN EOMs are depicted in **Figure 7**.

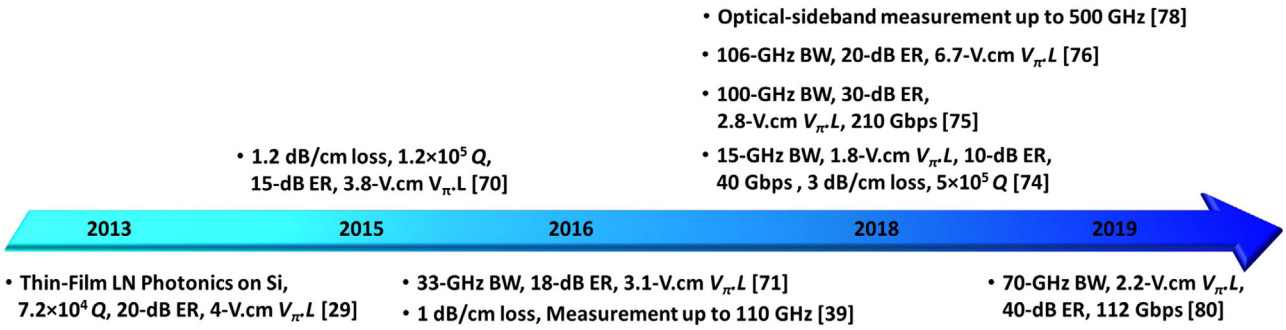

Figure 6. The timeline presents recent progress in TFLN EOMs in terms of key performance parameters, namely, LN waveguide propagation loss, 3-dB modulation BW, ER, and $V_\pi \cdot L$ at low frequencies. Q denotes the quality factor of TFLN microrings. The figure represents significant achievements in TFLN EOM technology and is not all-inclusive.

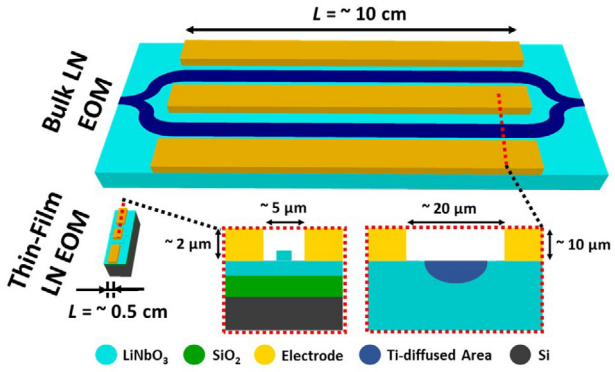

Figure 7. Comparison between conventional bulk LN versus ultracompact TFLN MZ EOMs. The 3D schematics are drawn to scale, in order to emphasize the significant reduction in the device footprint. The 2-D device cross-sections are not in scale. By utilizing the highly-compact optical mode in the TFLN case, the gap between the metallic electrodes can be decreased without inducing additional optical loss which results in lower $V_\pi \cdot L$ values compared to its bulk counterpart.

As mentioned in Section 2, TFLN on LN substrates was demonstrated in 2004.[30] Later on [122], it was shown that the material properties of bulk LN are preserved in TFLN platform, and an EOM with $V_\pi \cdot L$ of 15 V.cm and 15-20 dB cm^{-1} propagation loss was demonstrated for direct-etched Z-cut TFLN waveguides at 1550 nm wavelength. In BCB-bonded Z-cut TFLN, direct-etched microrings with quality factors, Q, of 10^3 to 10^4 were demonstrated in [63] and [21], respectively, and propagation loss as low as 7 dB cm^{-1} were reported.[21]

In 2013, our group at CREOL demonstrated the first wafer-scale TFLN on Si substrates.[29] The fabrication process for such wafers are summarized in Figure 2. By rib-loading the obtained TFLN with tantalum pentoxide (Ta_2O_5), MZ EOMs with remarkable $V_\pi \cdot L$ of 4 V.cm and 20 dB ER were attained. Decent propagation loss of 5 dB cm^{-1}, and a Q of $\sim 7.2 \times 10^4$ were also demonstrated for microrings. Moreover, by using the Y-cut TFLN, the largest EO coefficient of LN (r_{33}) was utilized by applying a lateral electric field along the Z-axis. In an improved report,[70] by rib-loading the same platform with ChG, MZ EOMs with $V_\pi \cdot L$ of 3.8 V.cm and gigahertz-range operation were demonstrated. Also, the propagation loss was reduced to 1.2 dB cm^{-1} and microrings with Q of $\sim 1.2 \times 10^5$ were reported.

Ultracompact TFLN waveguides with propagation loss as low as 0.2 dB cm^{-1} are achieved by Cai et al.,[53] by utilizing the mature PE process from bulk LN technology and applying it to the LNOI platform. This value was on par with the best propagation loss reported for conventional LN waveguides. However, as mentioned in Section 2.2, weak optical confinement and large bending radii of this platform impede ultracompact EOMs.

Our group reported on high-speed TFLN EOMs in 2016.[71] Characterized up to 50 GHz, the devices demonstrated 33-GHz 3-dB BW, $V_\pi \cdot L$ of 3.1 V.cm, and 18-dB ER in 8-mm-long devices (see **Figure 8a**). PECVD-Si_3N_4 was used for rib-loading the Y-cut TFLN, and waveguides with propagation loss of 1 dB cm^{-1} were reported.

In the same year, Mercante et al.[39] demonstrated a 10-mm-long TFLN phase modulator on Si substrate with ~40-GHz BW and ~1-dB cm^{-1} waveguide propagation loss. The fabrication of the device included less-favored approach of mechanical thinning an X-cut LN film and bonding it to Si substrate using an adhesive polymer. Nonetheless, careful RF design of the EOM (reducing the impedance and RF and optical index mismatch by partially etching the LN layer at the waveguides region and decreasing the thickness of the LN which possesses a large dielectric constant) ensured high-speed operation up to 110 GHz.

In 2017, Zhang et al.[46] demonstrated microrings with Q values up to ~10^7, and propagation loss of 0.027 dB cm^{-1} on an X-cut TFLN on Si platform. This work among a few others later on [47, 49], were significant achievements in low-loss direct-etching of LN.

In 2018, we reported on detailed general transmission-line modeling, and design guidelines for ultracompact TFLN EOMs predicting 100-GHz BW.[141] The main shortcoming with the commonly employed models in the literature which had been originally developed for bulk device was the impedance matching, typically assumed, between the EOM's transmission line properties and the terminating resistive load at all modulation frequencies. This was proved to not be applicable to compact EOMs. By comparison with our previous experimental data,[71] we showed that our EO modeling[141] is capable of accurate prediction of the device's EO response. Additionally, by optimization of device parameters, the model predicted that 100-GHz 3-dB BW is attainable in such ultracompact devices.

Later that year, Wang et al.[75] reported MZ EOMs with 100-GHz BW, 30-dB ER, $V_\pi \cdot L$ of 2.2 V.cm, and insertion loss of <1 dB

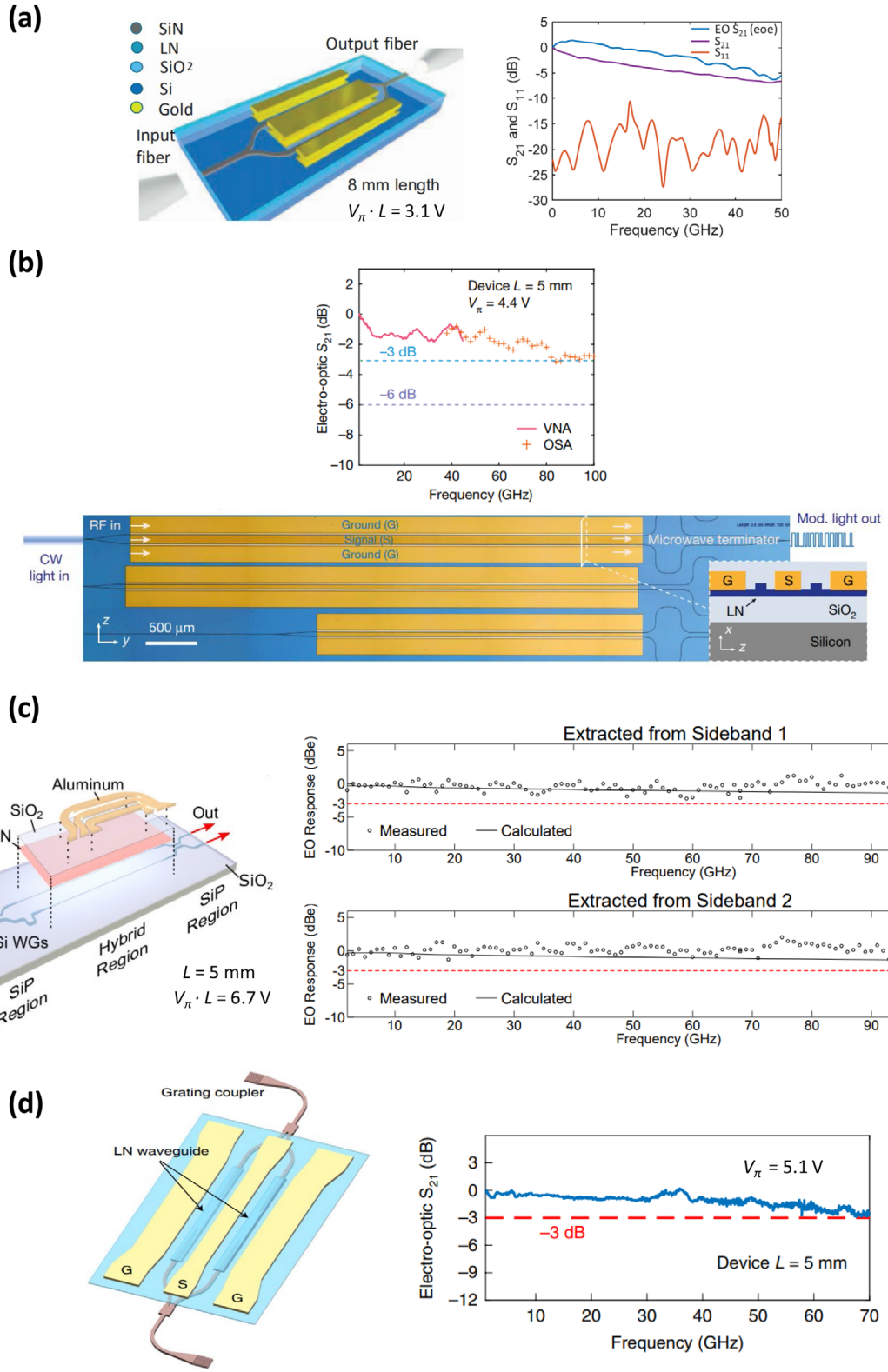

Figure 8. Examples of recent high-performance TFLN MZ EOMs on Si[71,75,76,80]: a) 18-dB ER, and 33-GHz BW. Reproduced with permission.[71] Copyright 2016, The Optical Society; b) 30-dB ER , and 100-GHz BW. Reproduced with permission.[75] Copyright 2016, Springer Nature; c) 20-dB ER, and 106-GHz BW. Reproduced with permission.[76] Copyright 2018, The Optical Society; d) 40-dB ER, and 70-GHz BW. Reproduced with permission.[80] Copyright 2016, Springer Nature. L is the modulation length. Values for V_π, and ER are reported at low frequencies.

Table 2. Summary of performance parameters for TFLN MZ EOMs. BW denotes the 3-dB electrical modulation BW. $V_\pi \cdot L$, and ER are at reported values at low frequencies. The values inside the parenthesis represent the reported measurements for another device in the same work.

TFLN platform (Year)	$V_\pi \cdot L$ [V.cm]	V_π [V]	L [mm]	BW [GHz]	ER [dB]	Reference
Dry-etched (2005)	15	42.8	3.5	N/A	N/A	[122]
Rib-loaded (2013)	4	6.8	6	N/A	20	[29]
Rib-loaded (2015)	3.8	6.3	6	1	15	[70]
Rib-loaded (2016)	3	2.5	12	8	13.8	[72]
Rib-loaded (2016)	3.1	3.87	8	33	18	[71]
Dry-etched (2018)	1.8	9	2	15	10	[74]
Dry-etched (2018)	2.2 (2.8)	4.4 (1.4)	5 (20)	100 (45)	N/A (30)	[75]
SOI-bonded (2018)	6.7	13.4	5	>106	20	[76]
Ti-diffused (2019)	7.2	1.2	60	20	40	[54]
SOI-bonded (2019)	2.55 (2.2)	5.1 (7.4)	5 (3)	70 (>70)	N/A (40)	[80]
SOI-bonded (2019)	2.5	2.5	10	50	16	[83]
Rib-loaded (2020)	6.7	13.4	5	30.6	20	[85]

in 5-mm-long devices on direct-etched *X*-cut TFLN on Si platform (see Figure 8b). Direct CMOS-driven modulation at 70 Gbit s^{-1} was demonstrated on 20-mm-long devices with ~45-GHz BW. Higher modulation speeds up to 210 Gbit s^{-1} were also presented with bit-error-ratio (BER) of 1.5×10^{-2}.

Also, Weigel et al.[76] reported on >106-GHz BW, 20-dB ER, $V_\pi \cdot L$ of 6.7 V.cm, and 7.6-dB insertion loss in 5-mm-long EOMs on a direct-bonded *X*-cut TFLN on to SOI waveguides (see Figure 8c). The 3-dB BW reported in this work is the highest experimentally demonstrated value up to date. The same group has recently showed 20 Gbit s^{-1} data modulation with eye-diagrams and signal-to-noise ratio measurements up to 102 GHz.[77]

In another TFLN EOM demonstration in 2018, Mercante et al.[78] demonstrated a direct-etched TFLN phase modulator on quartz substrate. The devices exhibited ~7-dB cm^{-1} propagation loss, and were characterized up to 500 GHz by optically-assisted methods. The 3-dB RF BW of this work, however, is limited to below 10 GHz.

While ~100 GHz remains the highest experimentally demonstrated BW to date,[75,76] we have recently reported on detailed optical and RF design techniques, which proves that up to 400-GHz 3-dB BW is attainable in ultracompact TFLN EOMs.[128] Such unprecedented BWs could find tremendous interest in a variety of system applications mentioned at the beginning of this section.

More recently, He et al.[80] have demonstrated TFLN MZ EOMs with 70-GHz BW, and $V_\pi \cdot L$ of 2.55 V.cm in 5-mm-long devices (see Figure 8d). $V_\pi \cdot L$ of 2.2 V.cm and ER of 40 dB and more are reported for 3-mm-long EOMs. Also, eye diagram measurements and BER values have been reported for high-speed modulations up to 112 Gbit s^{-1}. So far, the ER and $V_\pi \cdot L$ of this work are the best values reported for high-speed TFLN EOMs to date. However, it is worth mentioning that, recently, by cascading two TFLN MZ EOMs higher ER (up to 53 dB) has been demonstrated.[142] The devices in [80] are fabricated by using a BCB-bonding method of TFLN to SOI waveguides, as depicted in Figure 4. In addition, direct-etching of LN is also employed (see Figure 3h) in order to fully transfer the optical mode from SOI to LN waveguides in the modulator region compared to the partially-transferred optical mode in [76]. Clearly, more optical confinement in LN leads to an improved EO performance in the TFLN EOMs. This optical mode transitions are carried through vertical adiabatic couplers. The measured optical loss for each coupler is ~0.19 dB, and the overall insertion loss of the EOM is 2.5 dB. More recently, the same group has reported on a Michelson interferometer modulator on the same platform with 17.5-GHz BW, 30-dB ER, and a low $V_\pi \cdot L$ of 1.2 V.cm in 1-mm-long devices.[84]

It is also worthwhile mentioning that there are only few work among TFLN EOMs, which report on linearity for analog applications.[69,71,80,85] Spurious-free dynamic range (SFDR) is a figure of merit for measuring the linearity of EOMs in microwave photonics.[120] Values from ~90 to ~100 dB.$Hz^{2/3}$ have been reported in these four TFLN work,[69,71,80,85] which are still inferior to the best values reported for bulk LN EOMs (~120 dB.$Hz^{2/3}$).[143] Hence, it is expected that more works could emerge to improve SFDR of TFLN EOMs.

In summary, a comparison between the main performance parameters of the MZ EOMs discussed in this work is presented in **Table 2**.

For completeness, we mention that compact TFLN EOMs are not limited to MZ or phase modulators. Another type is resonance-based devices such as microring modulators (MMs). In principal, they can be formed on any of the platforms depicted in Figure 3. While they offer smaller device footprint, they are usually more prone to fabrication errors compared to other type of EOMs and provide less BW. The main figures of merit for MMs are Q, tunabilty, that is, the amount of spectral shift in microring's optical resonance per applied electrical field, ER, and 3-dB BW. A summary of reported TFLN resonance-based devices are presented in **Figure 9** and **Table 3**.

4. Nonlinear Optics on TFLN

Another widespread application domain for LN is nonlinear integrated photonic due to its high second-order nonlinear coefficient (d_{33} = 30 pm V^{-1}). Titanium in-diffusion[19] and proton

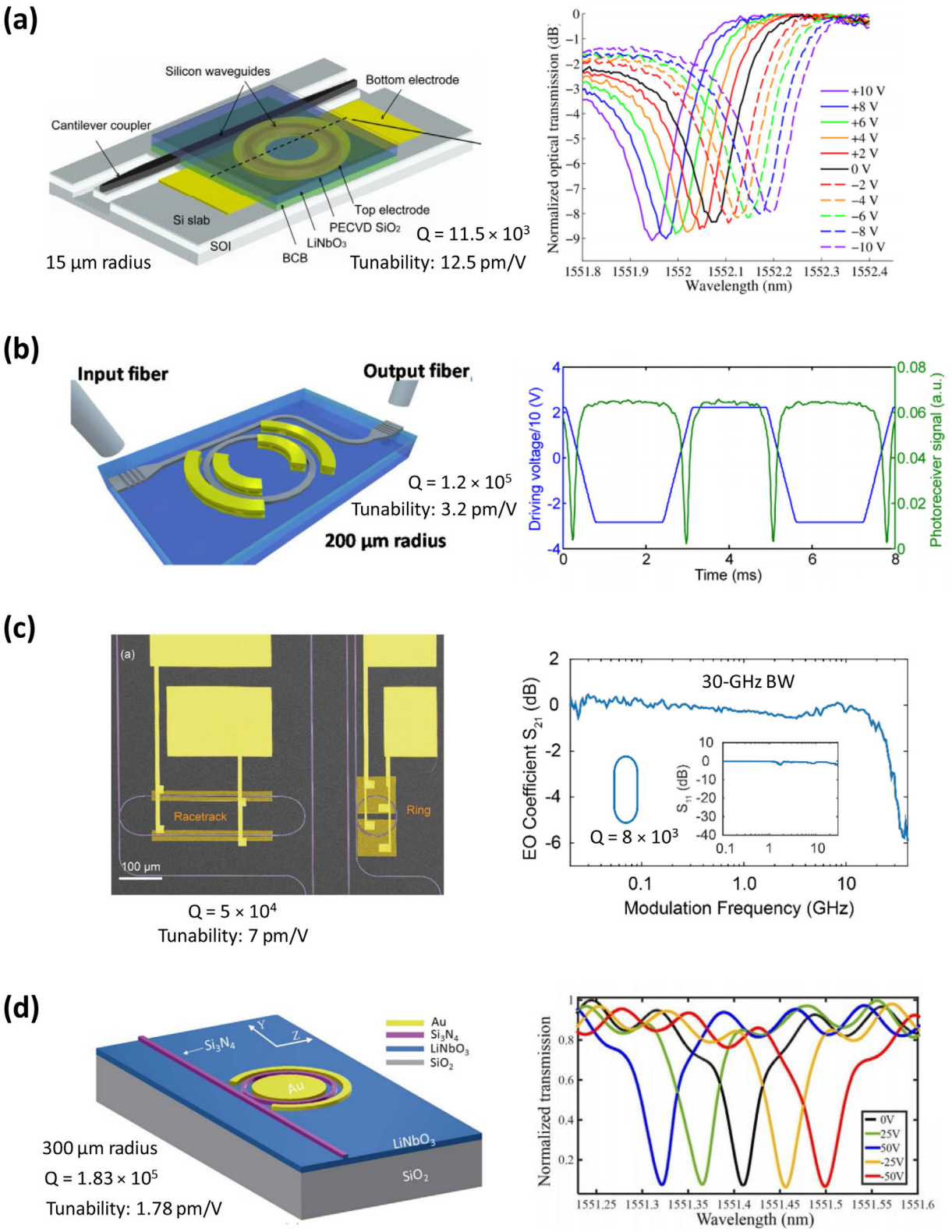

Figure 9. Examples of recently-demonstrated TFLN resonance-based EOMs[67,70,74,82]: a) BCB-bonded LN-SOI microring. Reproduced with permission.[67] Copyright 2013, The Optical Society; b) Rib-loaded LN-on-Si microring. Reproduced with permission.[70] Copyright 2015, The Optical Society; c) Dry-etched LN-on-LN microring. The racetrack resonator exhibits 3-dB BW of 30 GHz. Reproduced with permission.[74] Copyright 2018, The Optical Society; (d) Rib-loaded LN-on-quartz microring. Reproduced with permission.[81] Copyright 2019, The Optical Society.

Table 3. Summary of performance parameters for TFLN resonance-based EOMs. *R* and BW denote the radius, and 3-dB electrical modulation BW, respectively. The values for ER are at low frequencies.

TFLN Platform (Year)	*Q*	Tunability [pm V^{-1}]	*R* [μm]	ER [dB]	BW [GHz]	Reference
SOI-bonded (2007)	4×10^3	1.05	100	7	N/A	[63]
SOI-bonded (2011)	1.68×10^4	1.7	6	5	N/A	[37]
SOI-bonded (2013)	1.15×10^4	12.5	15	8	N/A	[67]
SOI-bonded (2014)	1.2×10^4	3.3	15	10	5	[68]
Rib-loaded (2015)	1.2×10^5	3.2	200	13	N/A	[70]
Dry-etched (2018)	8×10^3	7	N/A	N/A	30	[74]
Rib-loaded (2019)	1.85×10^5	1.78	300	27	N/A	[81]

exchange[20] have been the most commonly employed techniques in order to form LN waveguides, as previously discussed in Section 2.2. However, various limitations arise in these waveguides. which limit their performance and applicability to nonlinear integrated photonics. Low index contrast of the waveguide is a fundamental drawback that yields in a large cross-section and small overlap between the interacting modes. This limits the device performance due to high pump power required for the onset of second-order nonlinearity. On the other hand, large-scale integration can not be achieved with such devices due to their large device footprint.

TFLN platform is an excellent alternative that avoids the limitations of the predecessor approaches and demonstrates more compact and more efficient nonlinear integrated devices. On this platform, by employing rib-loading (see **Figure 3a**),[100,101] or direct-etching (see Figure 3b)[102,105] methods, high index contrast, and hence tight optical mode confinement, efficient modal overlap integral, and ultrahigh nonlinear conversion efficiency can be achieved. A variety of efficient nonlinear integrated devices have been recently demonstrated on this platform by various research groups, as elaborated in this section.

4.1. Periodically Poled TFLN Waveguides

Following the development of the TFLN technology, first periodically poled lithium niobate (PPLN) waveguides were demonstrated in 2016 using TFLN on Si and TFLN on LN platforms.[100,101] PPLN waveguides are conceptually wavelength converters that can be utilized for a variety of nonlinear processes such as, second-harmonic generation (SHG), difference-frequency generation (DFG) or sum-frequency generation (SFG).

A 3D schematic diagram of the PPLN device on Si is shown in Figure 10a with a SiN rib-loaded waveguide on Si substrate[100] along with optical mode simulation of the pump and SHG. This waveguide demonstrated 8% nonlinear conversion efficiency with pulsed laser pump around 1550-nm wavelength. A cross-section of TF-PPLN waveguide on LN substrate[101] is shown in Figure 10b with reported normalized nonlinear conversion efficiency of 160 $\%W^{-1}cm^{-2}$ in 4.8-mm-long device using continuous-wave pump around 1530-nm wavelength. This efficiency is more than 4 times larger than the typical values in conventional PPLNs, yet one order of magnitude less than the theoretical value, which is attributed to lateral leakage of the optical mode into the slab modes at SH wavelengths. A detailed study on this effect can be found in ref. [144].

Table 4. Examples of recently-demonstrated TF-PPLN devices. η and *L* represent the normalized conversion efficiency, and the length of the poled region, respectively. CAR denotes the coincidence-to-accidental ratio measurements for on-chip photon-pair generation.

TFLN Platform (Year)	η [$\%W^{-1}cm^{-2}$]	*L* [mm]	CAR	Reference
Rib-loaded (2016)	160	4.8	N/A	[101]
Rib-loaded (2016)	N/A	4	~300	[100, 112, 116]
Dry-etched (2018)	2600	4	N/A	[102]
Dry-etched (2019)	4600	0.6	~7000	[105, 113]
Dry-etched (2019)	2000	5	~67000	[115]
Dry-etched (2019)	2200	4	~600	[114]

As previously discussed in Section 2.2, dry etching *X*- and *Y*-cut LN waveguides have been historically challenging; however, various research groups have recently reported successful etching processes with low propagation loss.[46–49,102,105] These demonstrations have opened the door wide for realization of ultrahigh-efficiency TF-PPLN waveguides. Such a process has been first used to fabricate a 4-mm long PPLN waveguide, shown in Figure10c, with normalized conversion efficiency of 2600 $\%W^{-1}cm^{-2}$.[102] By utilizing an active iterative poling technique, our group at CREOL has recently demonstrated record-high 4600 $\%W^{-1}cm^{-2}$ normalized efficiency in 0.6-mm-long devices,[105] as shown in Figure10d. This efficiency is the highest reported normalized conversion efficiency to date and very close to the theoretical limit calculated for this type of waveguides. The TF-PPLN waveguides discussed above are summarized in **Table 4**.

In addition to standard PPLN devices, SHG has also been recently reported in *X*-cut and *Z*-cut PPLN microring resonators, with normalized conversion efficiency of 230 000 $\%W_{-1}$[106] and 250 000 $\%W_{-1}$,[107] respectively. This method has been achieved through careful design of a doubly-resonant device at the pump and the SHG wavelength using a single pulley waveguide. An example of such devices in *Z*-cut TFLN with the measured SHG spectrum is shown in **Figure 11**, while the pump laser is swept across the telecom band. Further optimization to decrease the propagation loss and increase the efficiency of these devices may enable nonlinearity at single-photon level, which will pave the path for interesting quantum-photonic applications such as

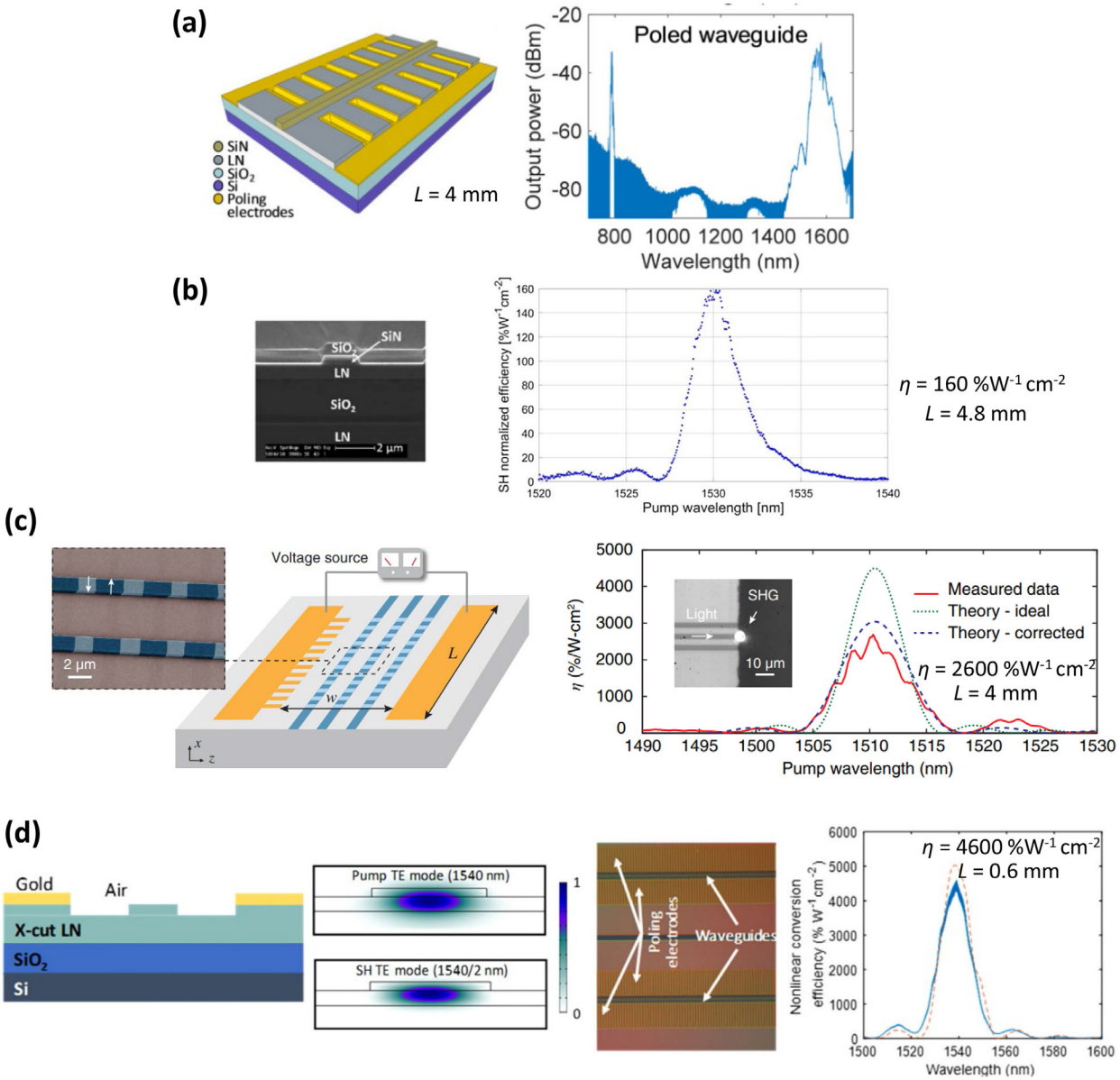

Figure 10. = Examples of recently-demonstrated TF-PPLN waveguides[100–102,105]: a) Rib-loaded TF-PPLN with nonlinear conversion efficiency of 8% for pulsed input. Reproduced with permission.[100] Copyright 2016, The Optical Society; b) Rib-loaded TF-PPLN. Reproduced with permission.[101] Copyright 2016, The Optical Society; c) Dry-etched TF-PPLN. Reproduced with permission.[102] Copyright 2018, The Optical Society; d) Dry-etched TF-PPLN. Reproduced with permission.[105] Copyright 2019, The Optical Society. η is the reported normalized conversion efficiency. L denotes the length of the poled region.

deterministic entanglement generation and control-NOT gate for single photons.[106]

Phase matching (momentum conservation) is a critical condition to be satisfied for realization of efficient PPLN waveguides. Various phase-matching techniques have been utilized in order to demonstrate TF-PPLN waveguides.[121] Among these, quasi-phase matching (QPM) may be considered as the most preferred approach.[144–149] The advantages include waveguide design and optimization freedom, as well as access to the largest nonlinear coefficient of LN (d_{33}). QPM is achieved in PPLN waveguides through inverting the crystalline domain polarity periodically to compensate for the wave-vector mismatch Δk between the pump and SHG optical modes. This has been historically realized in bulk PPLN by applying an electric field higher than the coercive (threshold) field value of ~21 kV/mm.[150] The same concept is used in TF-PPLN, but with higher threshold field value of ~30 – ~50 kV/mm. This higher required electric field can be attributed to the bonding interface between the TFLN and the SiO_2 insulating layer, or the out-diffusion of Li^+ during the annealing step of TFLN wafer fabrication process.[101,145]

Periodic poling by means of electric field is a powerful technique for domain inversion of ferroelectric materials, in order to achieve quasi-phase matching (QPM) for second-order ($\chi^{(2)}$) nonlinear processes. It does not suffer from drawbacks such

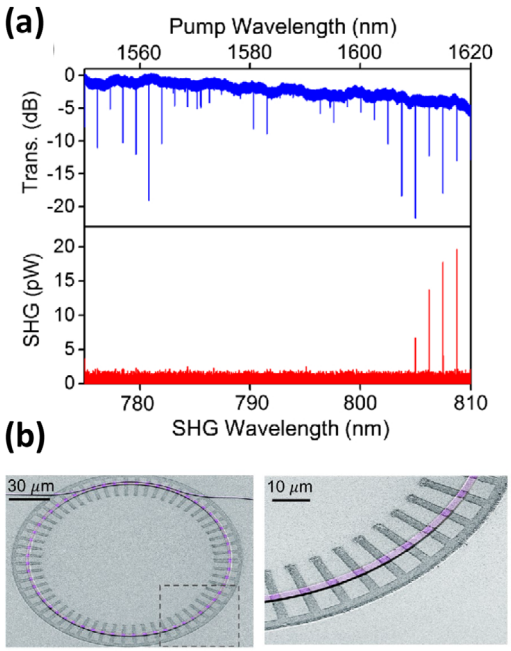

Figure 11. Demonstration of efficient SHG in PPLN microring resonators: a) SHG signal (red), when TE-polarized pump laser is swept across the telecom band (blue); b) False color SEM images of the etched device in hydrofluoric acid. Reproduced with permission.[107] Copyright 2019, The Optical Society.

as shallow inverted layers as in the chemical diffusion method or axial variation in domain periodicity in the crystal growth technique.[150] LN domain polarity is determined by the relative position of the metal ions (Li and Nb) to the oxygen layers and can be reversed by reorienting the crystal from one stable configuration to the other as depicted in Figure 1b. This can be achieved by applying an electric field higher than the coercive electric field of LN. Electric-field-driven poling process can be divided into four successive steps: 1) nucleation centers formation at the positive electrode, 2) tip propagation or domain growth along the z-axis of the crystal, 3) domain walls propagation in lateral directions, that is, x- and y- directions of the crystal, and 4) domains merging.[146]

Achieving 50% duty cycle and uniform periodicity of the periodic domain are critical factors in determining the overall efficiency of the nonlinear devices. Domain inversion in TFLN is usually realized through applying a square pulse or more efficiently a series of short pulses (~10–20 ms) as in **Figure 12c**, depicting the evolution of the inverted domain in both cases. Employing a series of short pulses for poling guarantees formation of enough nucleation centers, complete inversion of the domain, periodic domain uniformity, and high poling yield. This also avoids temperature rising and domain merging due to sidewall propagation. An example of a poling pulse is shown in Figure 12a along with the piezoresponse force microscope image of the resulting periodic domain Figure 12b with ~50% duty cycle and high yield.[145]

Our group has recently demonstrated an actively-monitored iterative poling technique that enables higher efficiencies than usually achieved using conventional passive techniques.[105] It utilizes an optically monitored iterative poling, depoling, and repoling sequence with a series of at least nine pulses in each poling cycle. The resulting efficiency measured during this process is shown in Figure 12d,e, which confirms increase of the efficiency with the number of poling pulses and poling cycles.

Other research groups have also demonstrated various nondestructive techniques for in situ monitoring of the periodic poling by SH confocal microscopy,[146,148] monitoring the variation in continuous-wave light transmission through waveguide[146] and piezoresponse force microscopy (PFM).[149] This active monitoring and optimization of poling conditions has recently facilitated achieving sub-micrometer periodicity by Zhao et al.[149], which can enable the development of short-wavelength nonlinear optical devices. More details on periodic poling of TFLN waveguides and various methods in order to study and improve domain inversion can be found in refs. [105, 144–149].

4.2. Other Approaches to Phase Matching in TFLN Waveguides

Other alternative approaches for phase matching have been successfully demonstrated for $\chi^{(2)}$ processes in TFLN, although with less conversion efficiency compared to PPLN method. Nonetheless, the advantage of these methods is that they are poling-free, hence fabrication and device preparation are simplified. Another advantage is that the techniques discussed in this section are not limited to ferroelectrics, and in principal, can be applied to other nonlinear materials.[151] Detailed mathematical derivations for different phase matching methods can be found in ref. [121].

Grating assisted quasi-phase matching (GA-QPM) (or mode-shape modulation[152]) is an example of such alternatives, in which periodic spatial modulation of waveguide parameters is utilized in order to induce a periodic variation in the nonlinear overlap integral.[152–154]

In ref. [152] (see **Figure 13a**), our group applied GA-QPM to the TFLN platform by employing a sinusoidal width perturbation of the rib-loaded waveguides with SiN. SHG with ~1 $\%W^{-1}cm^{-2}$ normalized conversion efficiency was demonstrated in 4.9-mm-long waveguides at 784 nm wavelength. An optimized width modulation pattern and a higher-refractive-index rib material can increase the conversion efficiency of such devices.

We have also reported on random QPM based on the GA-QPM technique and demonstrated SHG at 775-nm wavelength.[154] As shown in Figure 13b, the periodicity of the sinusoidal modulation of waveguide's width (created by dry etching TFLN) is chosen randomly. Random QPM has the benefit of overcoming the intrinsic bandwidth limitations imposed by uniform periodic perturbation.

In modal phase matching (MPM), a multi-mode waveguide is designed so that the wavevector of the mode at pump wavelength is matched with the wavevector of one of the higher order modes at SHG wavelength.[153,155] Wang et al.[153] reported on MPM and GA-QPM on TFLN platform and demonstrated SHG with 41 and 6.8 $\%W^{-1}cm^{-2}$ normalized conversion efficiency, in 1-mm-, and 0.5-mm-long waveguides, respectively. For the MPM case, first- and third-order transverse-electric (TE) modes of a waveguide with fixed width (see Figure 13c) were phase matched, while a periodically-grooved structure is used for GA-QPM, as depicted in Figure 13d. While MPM waveguides offer higher conversion efficiency and a simpler fabrication process than the GA-QPM

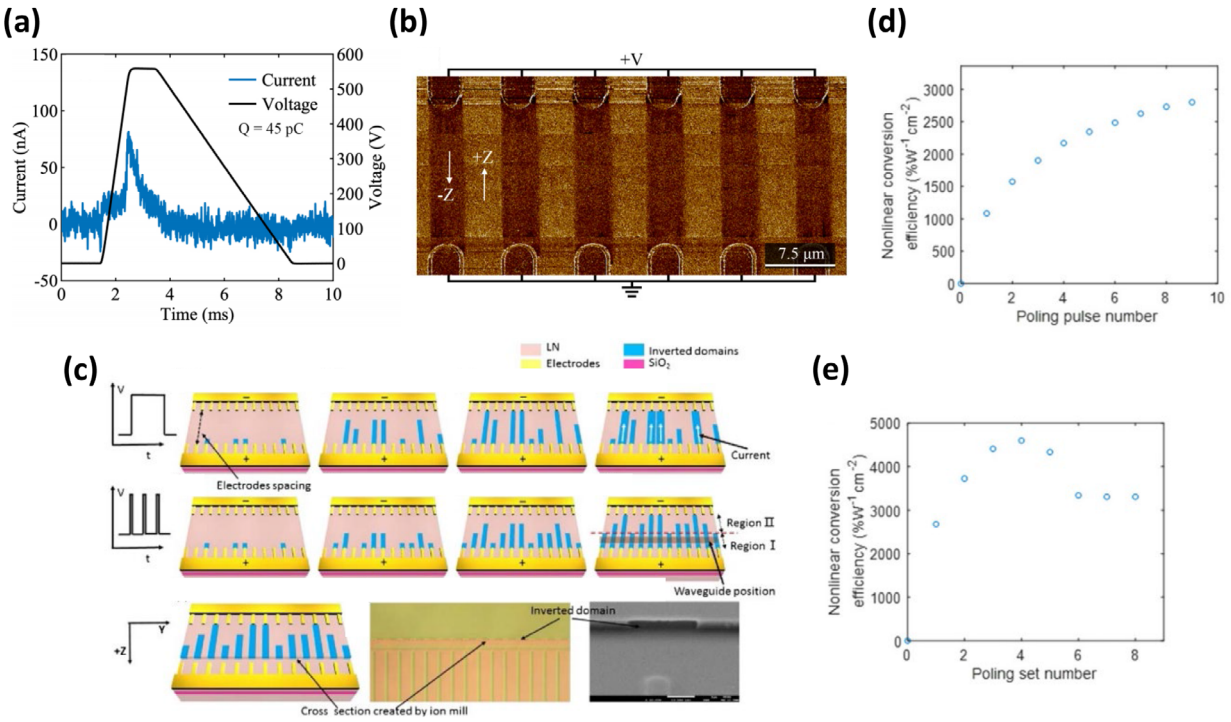

Figure 12. Periodic poling of TFLN waveguides: a) Example of poling pulse for TF-PPLN along with b) piezoresponse force microscope image of the resulting periodic domain. Reproduced with permission.[145] Copyright 2019, The Optical Society; c) Schematic illustration of the evolution of inverted domain using a long poling pulse and multi-pulse waveforms with short pulse durations. Images of the device are obtained after ion milling to visualize the periodically poled region. Reproduced with permission.[101] Copyright 2016, The Optical Society; Actively-monitored poling technique demonstrates increase of SHG efficiency with d) the number of poling pulses and e) the number of poling cycles, used for ferroelectric domain inversion (see Figure 1b). Reproduced with permission.[105] Copyright 2019, The Optical Society.

counterpart in this work, the GA-QPM method benefits from fundamental mode operation at both pump and signal wavelengths, similar to the PPLN devices in the previous section.

In general, the utilization of higher order modes have the drawbacks of less confinement and less overlap integral between the interacting optical modes. This results in higher propagation loss due to waveguide sidewall roughness and lower nonlinear efficiency. It is worth mentioning that for the case of microresonators, in addition the MPM method,[156] other techniques for phase matching have been also demonstrated, for example, cyclic phase matching.[157]

In another interesting poling-free MPM approach for SHG in TFLN platform, Luo et al.[158] have employed a heterogeneous TiO_2-LN waveguide structure, and demonstrated 36 $\%W^{-1}$ conversion efficiency corresponding to 650 $\%W^{-1}cm^{-2}$ normalized efficiency in 2.3-mm-long waveguides at 775-nm wavelength. By combining the thermooptic birefringence property of LN with MPM, the same group have demonstrated tunable SHG in TFLN platform with 0.84 nm K^{-1} tunability for a telecom-band pump with 4.7 $\%W^{-1}$ conversion efficiency in 8-mm-long waveguides.[159]

4.3. Other Nonlinear Applications of TFLN Waveguides

Applications of TFLN nonlinear devices include frequency meteorology, coherent optical communication links between the telecom and visible bands, optical frequency synthesizers, compression of ultrashort pulses required for studying solid-state material properties, frequency comb generation in LiDAR, and mid-infrared spectroscopy.[8,23,105,160] The high amount of optical power used in certain nonlinear applications can induce optical damage to the TFLN crystal.[161,162] This can be mitigated by employing adequate Magnesium Oxide (MgO) doping in TFLN similar to bulk LN crystals.[163] In this section, we present the different classical nonlinear applications whereas the quantum applications will be summarized later in Section 5.

SHG is the most straight forward nonlinear application of TFLN waveguides. As discussed earlier, TFLN platform has achieved ultrahigh efficient SHG devices. Difference-Frequency Generation (DFG) and Sum-Frequency Generation (SFG) are similar nonlinear applications that have been successfully demonstrated as well in TFLN waveguides. DFG has been recently reported in *X*-cut TF-PPLN waveguides with bandwidth more than 4.3 THz[114] and TFLN microdisks.[164] SFG has also been demonstrated by different groups either in TFLN waveguides[105,165] or TFLN microdisks.[60,166]

LN is a non-centrosymmetric material with small $\chi^{(3)}$ coefficient compared to its $\chi^{(2)}$. However, effective four-wave mixing, that is, Kerr nonlinearity, has been recently reported through cascaded SHG-DFG process in TFLN microdisk.[167] Third[105, 168–171] and fourth[105, 168, 169] harmonic generation have also been observed through similar cascaded nonlinear processes. Cascaded nonlinearity has enabled multi-octave supercontinuum

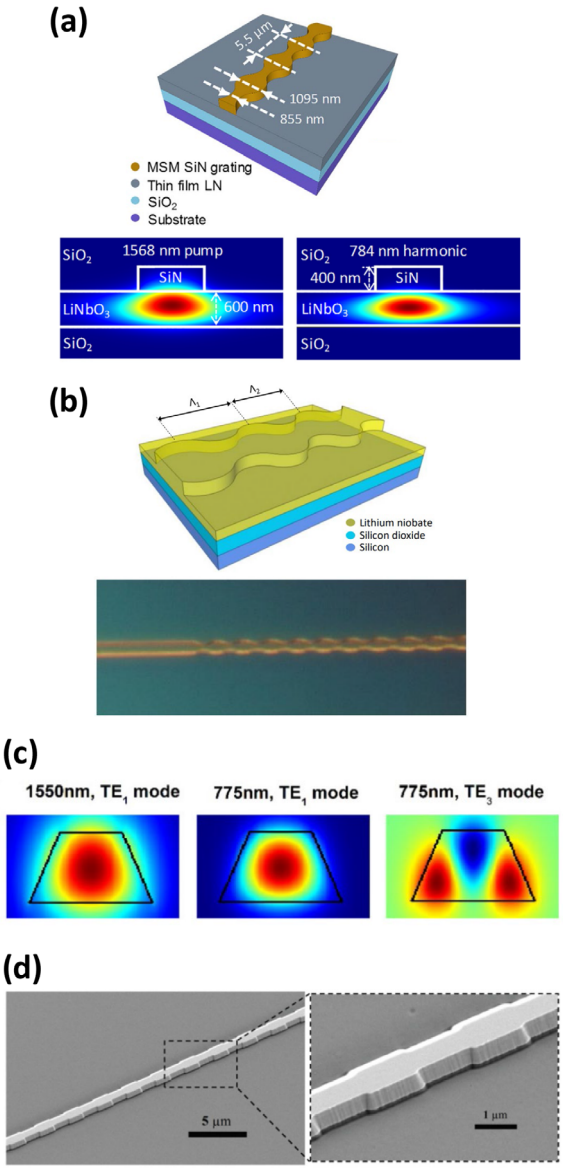

Figure 13. Demonstration of poling-free methods[152–154] for SHG in TFLN platform: a) 3-D schematic of a rib-loaded GA-QPM waveguide with a sinusoidal modulation of the width along with the optical mode profiles of the fundamental and second-harmonic TE modes at a grating width of 1095 nm. Reproduced with permission.[152] Copyright 2017, AIP Publishing; b) 3-D schematic of a random QPM waveguide on a dry-etched TFLN platform along with a micrograph of the fabricated device. Reproduced with permission.[154] Copyright 2018, The Optical Society; c) Optical mode profiles of the first- and third-order TE modes at the pump and second-harmonic wavelengths for MPM; d) SEM image of the fabricated GA-QPM structure. c,d) Reproduced with permission.[153] Copyright 2017, The Optical Society.

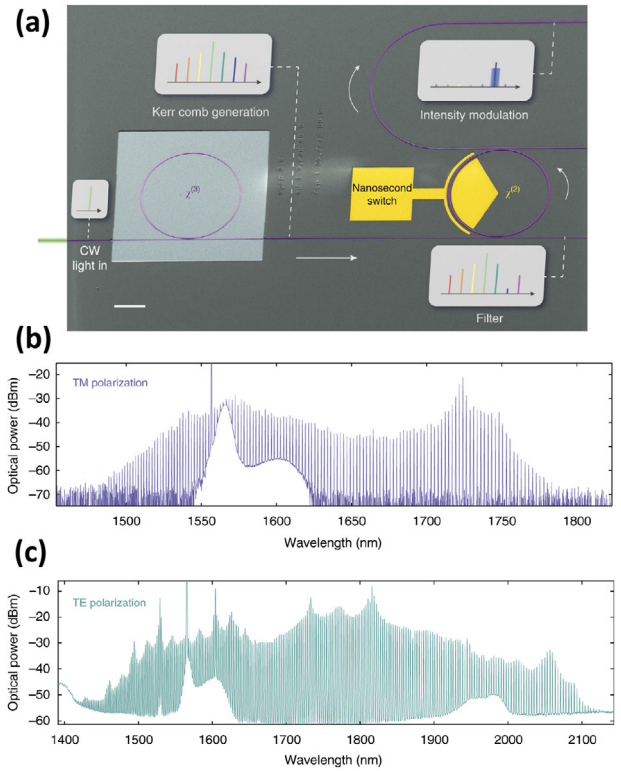

Figure 14. Demonstration of broadband Kerr frequency comb generation in the TFLN platform: a) False-color SEM image of the fabricated chip; Generated frequency comb spectra pumped at b) TM, and c) TE modes. Reproduced with permission.[110] Copyright 2019, Springer Nature.

generation in dispersion-engineered LN[103] and PPLN waveguides.[111] Second- and third-harmonic generation have been also recently reported in high-Q 2-D photonic crystals in X-cut TFLN.[172]

By employing high-Q microrings, Kerr frequency comb generation has also been proposed and demonstrated on the TFLN platform.[110,173–175] An example of such devices—pumped at telecom wavelengths and achieving up to ~700-nm comb spanning—is depicted in **Figure 14**.[110]

It is noted that frequency comb generation in the TFLN platform is not limited to Kerr nonlinearity discussed above. Another interesting approach is based on the EO effect.[109,135,176] A review of recent developments and various approaches for frequency comb generation in the TFLN platform can be found in ref. [133].

In addition to standalone nonlinear devices on TFLN platform, cascaded heterogeneous integration of other materials with higher $\chi^{(3)}$ nonlinearity, such as SiN and ChG, have been also pursued.[41,124,177] In ref. [124], we have addressed the fabrication challenges of cascaded integration of such materials by employing low-loss mode-converting tapers. This work paves the path toward providing efficient platform in order to realize multiple nonlinearity, that is, large $\chi^{(2)}$ of LN and high $\chi^{(3)}$ of ChG, on a single Si chip with applications like stabilized comb generation through *f*-to-2*f* carrier envelope offset (CEO) locking. In a recent work, Okawachi et al.[178] have demonstrated such an stabilized comb generation in a single dispersion-engineered TFLN waveguide.

In another application of TF-PPLN waveguides, we have recently employed our highly-efficient devices accompanied with spectral filtering, to build wide-band non-magnetic linear optical isolators with potential for monolithic integration of the whole system on a single chip.[179] This work could add an important piece to the component library of PICs, which enables building complete systems out of this platform only.

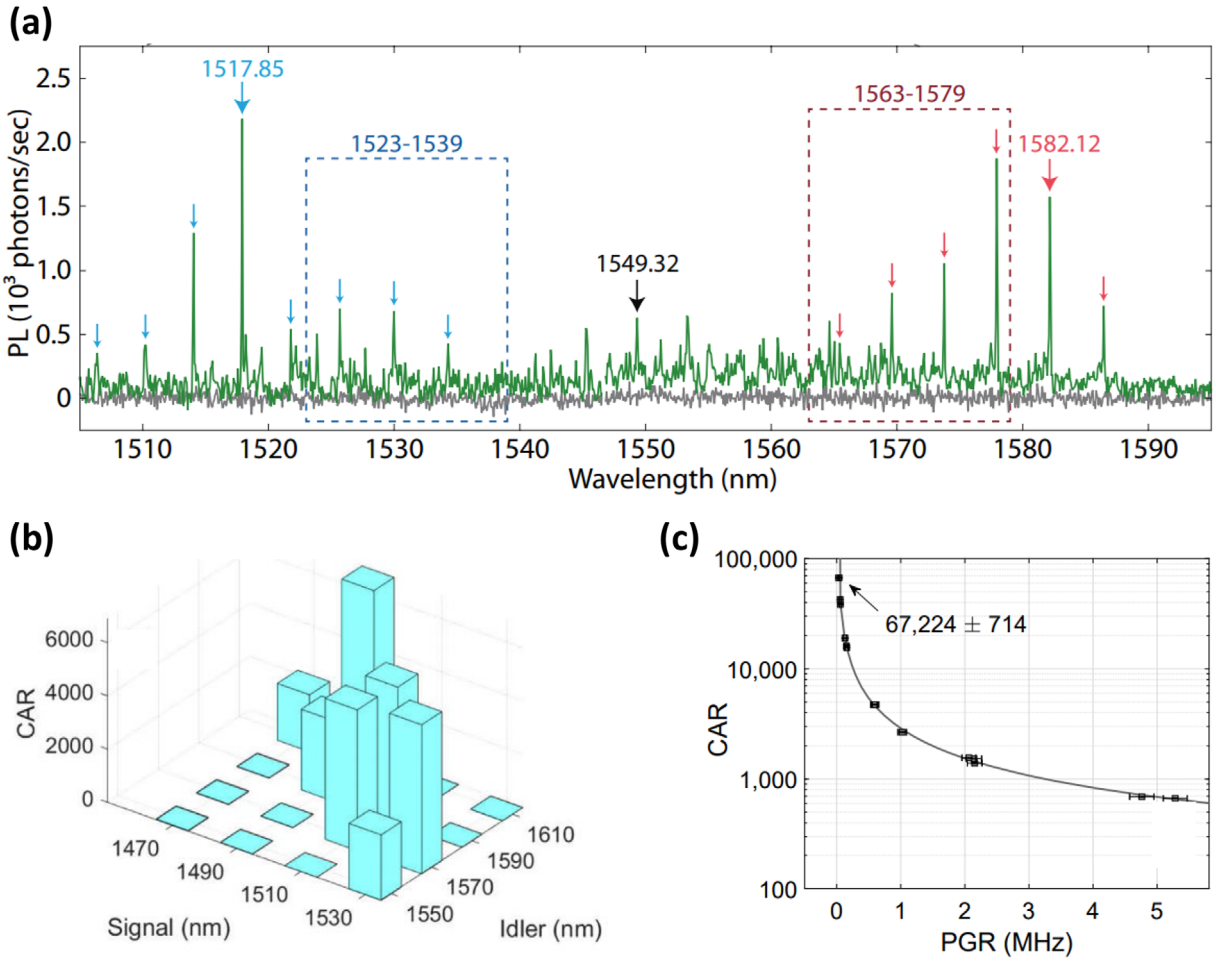

Figure 15. Examples of photon-pair generation demonstrated in TFLN platform: a) Wide-band (up to 400 nm) SPDC spectrum. Reproduced with permission.[157] Copyright 2017, The Optical Society; b) CAR values of up to 7000 with more than 120-nm signal-idler channel separation. Reproduced with permission.[113] Copyright 2019, The Optical Society; c) CAR values > 67000 at 82 kHz pair generation rate. Reproduced with permission.[115] Copyright 2020, American Physical Society.

5. Quantum Optics on TFLN

Integrated quantum photonic is an emerging field with promising applications in quantum computing and quantum optical communication.[180,181] The TFLN platform is a suitable candidate with a high potential for realization of complex quantum PICs due to its superior nonlinear and EO properties. This enables the generation and manipulation of non-classical light on chip.[182]

The first entangled photon pair sources in TF-PPLN on Si, based on the spontaneous parametric down conversion (SPDC) process, was demonstrated in 2018.[112,116] Pumped with a Ti-sapphire laser at 792 nm, with <0.5 ps pulse-width, and a repetition rate of 81.8 MHz, on-chip photon pair generation with rate of ~1 MHz mW^{-1} and a coincidence-to-accidental ratio (CAR) of 15 were demonstrated.[112] By utilizing a time-of-flight fiber spectrometer, we were able to spectrally resolve the second-order coherence of photon pairs on the same chip with CAR values of >300.[116] More recently, by using the aforementioned highly-efficient TF-PPLN devices,[105] broadband correlated photon-pair was generated in 300 μm-long-PPLN waveguides with a signal-idler channel separations of ~140 nm and CAR around 7000[113] (see **Figure 15b**). This work paves the path toward wide and continuous on-chip pair-matching for high channel capacities. Reducing the input/output coupling loss and improved filtering can result in much higher heralding efficiencies than the 3% reported in this work.

By incorporating longer TF-PPLN waveguides (5-mm-long poled region), Zhao et al.[115] have recently reported on CAR values >67 000 with 82 kHz generation rate, as depicted in Figure 15c. CAR values of the discussed work in this section are summarized in **Table 4**.

Figure 15c presents demonstrations of photon-pair generation in TFLN microdisks.[157] This device demonstrated a potential SPDC bandwidth over 400 nm inferred from the spectral measurements and a coincidence-to-accidental ratio (CAR) of 43. It is noted that due to the resonance-based operation of microdisks, the generated signal-idler pair spectrum is discrete whereas TF-PPLN devices are able to provide a continuous broadband spectrum which can be divided into various channels.[113]

TFLN has been also used recently to demonstrate waveguide-integrated superconducting nanowire single-photon detectors

(SNSPDs) with on-chip detection efficiency (OCDE) of 46%, a dark count rate of 13 Hz, and a timing jitter of 32 ps.[91] This has been achieved through the deposition of a thin-layer of niobium nitride (NbN) on top of the LN waveguide, which introduces the superconducting properties to TFLN platform. Achieving these devices is another important step toward the implementation of quantum PICs that generate, manipulate, process and measure quantum light.

We need to stress that integrated quantum photonics on TFLN platform is a still a young field with great potential but few reports to date. For discussion of previous work for conventional bulk LN waveguides, we refer the readers to the review in ref. [183]. It is expected that fully integrated quantum chips, such as those reported for conventional LN waveguides,[182,184] will be realized in the near future in TFLN platform with higher performance than their conventional LN counterparts due to improved modes confinement and smaller waveguide cross-sectional area.

6. Roadmap Ahead

In general, further improvement in terms of fiber-to-chip interface coupling,[92–99] careful consideration of electrical, RF, and optical packaging, and thermal/temporal reliability and stability studies are expected to be achieved soon for commercialization of fully-packaged TFLN devices. Heterogeneous integration of active elements such as lasers, amplifiers, and photodetecotrs along with various TFLN components on single photonic chip is another front which is expected to attract extensive research for a host of applications such as optical communication transceivers, high-performance computation, analog, digital, and quantum communication links, and LiDAR systems. In this regard, back end of line heterogeneous integration with SOI and SiN photonic circuitry seems to be the most anticipated scheme to be pursued for low-cost, large-scale, and foundry-compatible deployment of TFLN devices.

With such high levels of maturity for TFLN platform, the following advancements are expected to be achieved for each application reviewed in this work.

For the case of EOMs, achieving modulation BWs beyond 100 GHz is one of the next steps required for advanced communication systems. Studies have shown promising pathways for subterahertz application of EOMs.[78,128] However, it should be noted that full realization of integrated EOMs with such unprecedented BWs will require development of ultrahigh-speed electronic and photonic drivers and detection components as well. Another crucial milestone would be realization of higher modulation formats for coherent optical communication, which is yet to be demonstrated in TFLN platform.

Demonstration of nonlinear devices on TFLN with better performance is to be pursued in the near futures, through decreasing insertion and propagation losses, achieving the optimum poling conditions for PPLN waveguides or increasing the efficiency of other phase-matched waveguides. Incorporating standalone nonlinear devices into more system-like applications, such as our optical isolators, is also a promising direction to be followed. Heterogeneous integration of $\chi^{(3)}$ materials onto TFLN and cascaded nonlinearity using this heterogeneous platform is also a promising direction that paves the path for a variety of interesting applications such as highly efficient high-harmonic generation, frequency-stabilized optical frequency combs and generation of mid-infrared wavelengths.

More complex quantum PICs for generation and manipulation of single- and entangled-photon states are expected to be realized on LN. This is due to the fact that LN is combining linear (e.g., power splitters and combiners, wavelength division multiplexers), nonlinear (SHG and SPDC) functions and fast EO modulation. Entangled photon states, such as tripartite Greenberger-Horne-Zeilinger (GHZ), may also be attained in TFLN platform through cascading nonlinear devices on the same platform, with optimized ultrahigh nonlinear efficiency to realize high generation rate of these non-classical states. other non-classical applications such as entanglement swapping and heralded single photon sources with better efficiency are yet to be realized in TFLN. All of these demonstration will eventually enable the realization of quantum key distribution links, a crucial step for quantum secure communication.

7. Concluding Remarks

Diverse material features and excellent optical properties of LN have been extensively studied over the past decades. This versatile material has been one of the most attractive photonic platforms especially for electrooptic modulator and wavelength converter markets.

Recently, with the emergence of thin-film LN technology, the challenges and drawbacks of bulk LN have been overcome and standalone TFLN devices are outperforming their conventional bulk counterparts in terms of key performance parameters, such as waveguide propagation loss, modulation BW for EOMs, and conversion efficiency in the case of wavelength converters. In addition to performance boost, the TFLN technology is providing dramatic reduction in power consumption and overall device footprint in order to address the ever-increasing demands of large-scale integration in modern electronic-photonic systems.

In this paper, we have reviewed the most recent advancements of this flourishing technology. Key performance parameters of the main discussed applications, namely electro-, nonlinear-, and quantum-optics, are summarized in Tables 2–4. Thanks to successful commercialization of TFLN technology, a plethora of ultracompact photonic components and devices have been demonstrated on this platform. The overall efforts have rejuvenated LN for the major photonic applications focused in this work, as well as other optical and RF/MEMS applications (see Figure 1a) not discussed here.

Conflict of Interest

The authors declare no conflict of interest.

Keywords

electrooptic modulators, heterogeneous integration, integrated photonics, nonlinear photonics, quantum optics, silicon photonics, thin-film lithium niobate

Received: March 9, 2020
Revised: May 20, 2020
Published online:

[1] K. Nassau, Early history of lithium niobate: personal reminiscences, in: *Processing of Guided Wave Optoelectronic Materials I*, (**1984**), pp. 2–5.
[2] R. Weis, T. Gaylord, *Appl. Phys. A* **1985**, *37*, 191.
[3] K. K. Wong, *Properties of Lithium Niobate*, No. 28, IET **2002**.
[4] S. Fathpour, *Nanophotonics* **2015**, *4*, 143.
[5] R. C. Miller, W. A. Nordland, P. M. Bridenbaugh, *J. Appl. Phys.* **1971**, *42*, 4145.
[6] A. Bartasyte, S. Margueron, T. Baron, S. Oliveri, P. Boulet, *Adv. Mater. Interfaces* **2017**, *4*, 1600998.
[7] E. L. Wooten, K. M. Kissa, A. Yi-Yan, E. J. Murphy, D. A. Lafaw, P. F. Hallemeier, D. Maack, D. V. Attanasio, D. J. Fritz, G. J. McBrien, D. E. Bossi, *IEEE J. Sel. Top. Quantum Electron.* **2000**, *6*, 69.
[8] A. Rao, S. Fathpour, *IEEE J. Sel. Top. Quantum Electron.* **2018**, *24*, 1.
[9] [Online], www.thorlabs.com/navigation.cfm?guide_id=2218.
[10] [Online], Available: https://photonics.ixblue.com/store/lithium-niobate-electro-optic-modulator/intensity-modulators.
[11] [Online], Available: https://www.eospace.com/40-gb/s-modulators.
[12] [Online], Available: https://www.hcphotonics.com/ppln-chips.
[13] [Online], Available: www.covesion.com/products/magnesium-doped-ppln-mgoppln-crystals/mgo-ppln-for-second-harmonic-generation/mshg1550-0.5.html.
[14] [Online], Available: http://www.psicorp.com/products/rf-and-optical-components/periodically-poled-lithium-niobate-ppln-frequency-converter.
[15] B. Jalali, S. Fathpour, *J. Lightwave Technol.* **2006**, *24*, 4600.
[16] J. E. Bowers, T. Komljenovic, M. Davenport, J. Hulme, A. Y. Liu, C. T. Santis, A. Spott, S. Srinivasan, E. J. Stanton, C. Zhang, Recent advances in silicon photonic integrated circuits, in: *Next-Generation Optical Communication: Components, Sub-Systems, and Systems V*, edited by G. Li and X. Zhou (SPIE, **2016**), pp. 1–18.
[17] A. H. Atabaki, S. Moazeni, F. Pavanello, H. Gevorgyan, J. Notaros, L. Alloatti, M. T. Wade, C. Sun, S. A. Kruger, H. Meng, K. Al Qubaisi, I. Wang, B. Zhang, A. Khilo, C. V. Baiocco, M. A. Popovic, V. M. Stojanovic, R. J. Ram, *Nature* **2018**, *556*, 349.
[18] M. Teng, A. Honardoost, Y. Alahmadi, S. S. Polkoo, K. Kojima, H. Wen, C. K. Renshaw, P. LiKamWa, G. Li, S. Fathpour, R. Safian, L. Zhuang, *J. Lightwave Technol.* **2020**, *38*, 6.
[19] K. Noguchi, O. Mitomi, H. Miyazawa, *J. Lightwave Technol.* **1998**, *16*, 615.
[20] P. G. Suchoski, T. K. Findakly, F. J. Leonberger, *Opt. Lett.* **1988**, *13*, 1050.
[21] G. Poberaj, H. Hu, W. Sohler, P. Günter, *Laser Photonics Rev.* **2012**, *6*, 488.
[22] A. Boes, B. Corcoran, L. Chang, J. Bowers, A. Mitchell, *Laser Photonics Rev.* **2018**, *12*, 1700256.
[23] M. Rusing, P. O. Weigel, J. Zhao, S. Mookherjea, *IEEE Nanotechnol. Magazine* **2019**, *13*, 18.
[24] W. Sohler, B. K. Das, D. Dey, S. Reza, H. Suche, R. Ricken, *IEICE Transact. Electron.* **2005**, *88*, 990.
[25] D. Brüske, S. Suntsov, C. E. Rüter, D. Kip, *Opt. Express* **2019**, *27*, 8884.
[26] M. R. H. Sarker, H. Karim, R. Martinez, N. Love, Y. Lin, *IEEE Sens. J.* **2016**, *16*, 5883.
[27] K. Buse, A. Adibi, D. Psaltis, *Nature* **1998**, *393*, 665.
[28] V. Gopalan, V. Dierolf, D. A. Scrymgeour, *Annu. Rev. Mater. Res.* **2007**, *37*, 449.
[29] P. Rabiei, J. Ma, S. Khan, J. Chiles, S. Fathpour, *Opt. Express* **2013**, *21*, 25573.
[30] P. Rabiei, P. Günter, *Appl. Phys. Lett.* **2004**, *85*, 4603.
[31] M. Levy, R. M. Osgood, R. Liu, L. E. Cross, G. S. Cargill, A. Kumar, H. Bakhru, *Appl. Phys. Lett.* **1998**, *73*, 2293.
[32] H. Takagi, R. Maeda, N. Hosoda, T. Suga, *Appl. Phys. Lett.* **1999**, *74*, 2387.
[33] M. M. R. Howlader, T. Suga, M. J. Kim, *Appl. Phys. Lett.* **2006**, *89*, 031914.
[34] [Online], Available: http://www.partow-tech.com/.
[35] [Online], Available: https://www.nanoln.com/.
[36] [Online], Available: https://www.ngk-insulators.com/en/index.html.
[37] Y. S. Lee, G. D. Kim, W. J. Kim, S. S. Lee, W. G. Lee, W. H. Steier, *Opt. Lett.* **2011**, *36*, 1119.
[38] P. O. Weigel, M. Savanier, C. T. DeRose, A. T. Pomerene, A. L. Starbuck, A. L. Lentine, V. Stenger, S. Mookherjea, *Sci. Rep.* **2016**, *6*, 22301.
[39] A. J. Mercante, P. Yao, S. Shi, G. Schneider, J. Murakowski, D. W. Prather, *Opt. Express* **2016**, *24*, 15590.
[40] S. Li, L. Cai, Y. Wang, Y. Jiang, H. Hu, *Opt. Express* **2015**, *23*, 24212.
[41] L. Chang, M. H. P. Pfeiffer, N. Volet, M. Zervas, J. D. Peters, C. L. Manganelli, E. J. Stanton, Y. Li, T. J. Kippenberg, J. E. Bowers, *Opt. Lett.* **2017**, *42*, 803.
[42] Y. Wang, Z. Chen, H. Hu, *Crystals* **2018**, *8*, 191.
[43] A. N. R. Ahmed, A. Mercante, S. Shi, P. Yao, D. W. Prather, *Opt. Lett.* **2018**, *43*, 4140.
[44] D. Liu, L. Feng, Y. Jia, H. Ma, *Opt. Commun.* **2019**, *436*, 1.
[45] G. Ulliac, V. Calero, A. Ndao, F. Baida, M. P. Bernal, *Opt. Mater.* **2016**, *53*, 1.
[46] M. Zhang, C. Wang, R. Cheng, A. Shams-Ansari, M. Lončar, *Optica* **2017**, *4*, 1536.
[47] I. Krasnokutska, J. L. J. Tambasco, X. Li, A. Peruzzo, *Opt. Express* **2018**, *26*, 897.
[48] X. P. Li, K. X. Chen, Z. F. Hu, *Opt. Mater. Express* **2018**, *8*, 1322.
[49] L. Cai, A. Mahmoud, G. Piazza, *Opt. Express* **2019**, *27*, 9794.
[50] Q. Xu, Y. X. Shao, R. Q. Piao, F. Chen, X. Wang, X. F. Yang, W. H. Wong, E. Y. B. Pun, D. L. Zhang, *Adv. Theory Simul.* **2019**, *2*, 1900115.
[51] R. Geiss, S. Saravi, A. Sergeyev, S. Diziain, F. Setzpfandt, F. Schrempel, R. Grange, E. B. Kley, A. Tünnermann, T. Pertsch, *Opt. Lett.* **2015**, *40*, 2715.
[52] L. Cai, S. L. H. Han, H. Hu, *Opt. Express* **2015**, *23*, 1240.
[53] L. Cai, R. Kong, Y. Wang, H. Hu, *Opt. Express* **2015**, *23*, 29211.
[54] Y. Yamaguchi, A. Kanno, N. Yamamoto, T. Kawanishi, Experimental evaluation of wavelength-dependence of thin-film linbo3 modulator with an extinction-ratio-tunable structure, in: 2019 24th OptoElectronics and Communications Conference (OECC) and 2019 International Conference on Photonics in Switching and Computing (PSC), (July **2019**), pp. 1–3.
[55] L. Chen, J. Nagy, R. M. Reano, *Opt. Mater. Express* **2016**, *6*, 2460.
[56] R. Takigawa, T. Asano, *Opt. Express* **2018**, *26*, 24413.
[57] L. Cao, A. Aboketaf, Z. Wang, S. Preble, *Opt. Commun.* **2014**, *330*, 40.
[58] N. Courjal, B. Guichardaz, G. Ulliac, J. Y. Rauch, B. Sadani, H. H. Lu, M. P. Bernal, *J. Phys. D: Appl. Phys.* **2011**, *44*, 305101.
[59] J. Wang, F. Bo, S. Wan, W. Li, F. Gao, J. Li, G. Zhang, J. Xu, *Opt. Express* **2015**, *23*, 23072.
[60] Z. Hao, J. Wang, S. Ma, W. Mao, F. Bo, F. Gao, G. Zhang, J. Xu, *Photon. Res.* **2017**, *5*, 623.
[61] L. Wang, C. Wang, J. Wang, F. Bo, M. Zhang, Q. Gong, M. Lončar, Y. F. Xiao, *Opt. Lett.* **2018**, *43*, 2917.
[62] L. Zhang, D. Zheng, W. Li, F. Bo, F. Gao, Y. Kong, G. Zhang, J. Xu, *Opt. Express* **2019**, *27*, 33662.

[63] A. Guarino, G. Poberaj, D. Rezzonico, R. Degl'Innocenti, P. Günter, *Nat. Photonics* **2007**, *1*, 407.
[64] Y. He, H. Liang, R. Luo, M. Li, Q. Lin, *Opt. Express* **2018**, *26*, 16315.
[65] R. Wolf, I. Breunig, H. Zappe, K. Buse, *Opt. Express* **2018**, *26*, 19815.
[66] M. Bahadori, Y. Yang, L. L. Goddard, S. Gong, *Opt. Express* **2019**, *27*, 22025.
[67] L. Chen, M. G. Wood, R. M. Reano, *Opt. Express* **2013**, *21*, 27003.
[68] L. Chen, Q. Xu, M. G. Wood, R. M. Reano, *Optica* **2014**, *1*, 112.
[69] L. Chen, J. Chen, J. Nagy, R. M. Reano, *Opt. Express* **2015**, *23*, 13255.
[70] A. Rao, A. Patil, J. Chiles, M. Malinowski, S. Novak, K. Richardson, P. Rabiei, S. Fathpour, *Opt. Express* **2015**, *23*, 22746.
[71] A. Rao, A. Patil, P. Rabiei, A. Honardoost, R. DeSalvo, A. Paolella, S. Fathpour, *Opt. Lett.* **2016**, *41*, 5700.
[72] S. Jin, L. Xu, H. Zhang, Y. Li, *IEEE Photonics Technol. Lett.* **2016**, *28*, 736.
[73] M. Mahmoud, C. Bottenfield, L. Cai, G. Piazza, Fully integrated lithium niobate electro-optic modulator based on asymmetric mach-zehnder interferometer etched in lnoi platform, in: 2017 IEEE Photonics Conference (IPC), (Oct **2017**), pp. 223–224.
[74] C. Wang, M. Zhang, B. Stern, M. Lipson, M. Lončar, *Opt. Express* **2018**, *26*, 1547.
[75] C. Wang, M. Zhang, X. Chen, M. Bertrand, A. Shams-Ansari, S. Chandrasekhar, P. Winzer, M. Lončar, *Nature* **2018**, *562*, 101.
[76] P. O. Weigel, J. Zhao, K. Fang, H. Al-Rubaye, D. Trotter, D. Hood, J. Mudrick, C. Dallo, A. T. Pomerene, A. L. Starbuck, C. T. DeRose, A. L. Lentine, G. Rebeiz, S. Mookherjea, *Opt. Express* **2018**, *26*, 23728.
[77] X. Wang, P. O. Weigel, J. Zhao, M. Ruesing, S. Mookherjea, *APL Photonics* **2019**, *4*, 096101.
[78] A. J. Mercante, S. Shi, P. Yao, L. Xie, R. M. Weikle, D. W. Prather, *Opt. Express* **2018**, *26*, 14810.
[79] T. Ren, M. Zhang, C. Wang, L. Shao, C. Reimer, Y. Zhang, O. King, R. Esman, T. Cullen, M. Lončar, *IEEE Photonics Technol. Lett.* **2019**, *31*, 889.
[80] M. He, M. Xu, Y. Ren, J. Jian, Z. Ruan, Y. Xu, S. Gao, S. Sun, X. Wen, L. Zhou, L. Liu, C. Guo, H. Chen, S. Yu, L. Liu, X. Cai, *Nat. Photonics* **2019**, *13*, 359.
[81] A. N. R. Ahmed, S. Shi, M. Zablocki, P. Yao, D. W. Prather, *Opt. Lett.* **2019**, *44*, 618.
[82] A. N. R. Ahmed, S. Shi, A. J. Mercante, D. W. Prather, *Opt. Express* **2019**, *27*, 30741.
[83] V. Stenger, A. Pollick, C. Acampado, Integrable thin film lithium niobate (tfln™) on silicon electro-optic modulators, in: Optical Fiber Communication Conference (OFC) 2019, (Optical Society of America, **2019**), p. Tu2H.6.
[84] M. Xu, W. Chen, M. He, X. Wen, Z. Ruan, J. Xu, L. Chen, L. Liu, S. Yu, X. Cai, *APL Photonics* **2019**, *4*, 100802.
[85] N. Boynton, H. Cai, M. Gehl, S. Arterburn, C. Dallo, A. Pomerene, A. Starbuck, D. Hood, D. C. Trotter, T. Friedmann, C. T. DeRose, A. Lentine, *Opt. Express* **2020**, *28*, 1868.
[86] L. Shao, M. Yu, S. Maity, N. Sinclair, L. Zheng, C. Chia, A. Shams-Ansari, C. Wang, M. Zhang, K. Lai, M. Lončar, *Optica* **2019**, *6*, 1498.
[87] L. Cai, A. Mahmoud, M. Khan, M. Mahmoud, T. Mukherjee, J. Bain, G. Piazza, *Photon. Res.* **2019**, *7*, 1003.
[88] M. Khan, A. Mahmoud, L. Cai, M. Mahmoud, T. Mukherjee, J. A. Bain, G. Piazza, *J. Lightwave Technol.* **2019**, 1.
[89] L. Shao, N. Sinclair, J. Leatham, Y. Hu, M. Yu, T. Turpin, D. Crowe, M. Loncar, *arXiv preprint arXiv:2005.03794* (**2020**).
[90] B. Desiatov, M. Lončar, *Appl. Phys. Lett.* **2019**, *115*, 121108.
[91] A. A. Sayem, R. Cheng, S. Wang, H. X. Tang, *Appl. Phys. Lett.* **2020**, *116*, 151102.
[92] Z. Chen, R. Peng, Y. Wang, H. Zhu, H. Hu, *Opt. Mater. Express* **2017**, *7*, 4010.
[93] Z. Chen, Y. Wang, H. Zhang, H. Hu, *Opt. Mater. Express* **2018**, *8*, 1253.
[94] L. Cai, G. Piazza, *J. Opt.* **2019**, *21*, 065801.
[95] A. Kar, M. Bahadori, S. Gong, L. L. Goddard, *Opt. Express* **2019**, *27*, 15856.
[96] I. Krasnokutska, R. J. Chapman, J. L. J. Tambasco, A. Peruzzo, *Opt. Express* **2019**, *27*, 17681.
[97] L. He, M. Zhang, A. Shams-Ansari, R. Zhu, C. Wang, L. Marko, *Opt. Lett.* **2019**, *44*, 2314.
[98] I. Krasnokutska, J. L. J. Tambasco, A. Peruzzo, *Opt. Express* **2019**, *27*, 16578.
[99] N. Yao, J. Zhou, R. Gao, J. Lin, M. Wang, Y. Cheng, W. Fang, L. Tong, *Opt. Express* **2020**, *28*, 12416.
[100] A. Rao, M. Malinowski, A. Honardoost, J. R. Talukder, P. Rabiei, P. Delfyett, S. Fathpour, *Opt. Express* **2016**, *24*, 29941.
[101] L. Chang, Y. Li, N. Volet, L. Wang, J. Peters, J. E. Bowers, *Optica* **2016**, *3*, 531.
[102] C. Wang, C. Langrock, A. Marandi, M. Jankowski, M. Zhang, B. Desiatov, M. M. Fejer, M. Lončar, *Optica* **2018**, *5*, 1438.
[103] M. Yu, B. Desiatov, Y. Okawachi, A. L. Gaeta, M. Lončar, *Opt. Lett.* **2019**, *44*, 1222.
[104] T. Ding, Y. Zheng, X. Chen, *Opt. Lett.* **2019**, *44*, 1524.
[105] A. Rao, K. Abdelsalam, T. Sjaardema, A. Honardoost, G. F. Camacho-Gonzalez, S. Fathpour, *Opt. Express* **2019**, *27*, 25920.
[106] J. Y. Chen, Z. H. Ma, Y. M. Sua, Z. Li, C. Tang, Y. P. Huang, *Optica* **2019**, *6*, 1244.
[107] J. Lu, J. B. Surya, X. Liu, A. W. Bruch, Z. Gong, Y. Xu, H. X. Tang, *Optica* **2019**, *6*, 1455.
[108] R. Luo, Y. He, H. Liang, M. Li, Q. Lin, *Laser Photonics Rev.* **2019**, *13*, 1800288.
[109] M. Zhang, B. Buscaino, C. Wang, A. Shams-Ansari, C. Reimer, R. Zhu, J. M. Kahn, M. Lončar, *Nature* **2019**, *568*, 373.
[110] C. Wang, M. Zhang, M. Yu, R. Zhu, H. Hu, M. Loncar, *Nat. Commun.* **2019**, *10*, 1.
[111] M. Jankowski, C. Langrock, B. Desiatov, A. Marandi, C. Wang, M. Zhang, C. R. Phillips, M. Lončar, M. M. Fejer, *Optica* **2020**, *7*, 40.
[112] A. Rao, N. Nader, M. J. Stevens, T. Gerrits, O. S. Magaña-Loaiza, G. F. Camacho-González, J. Chiles, A. Honardoost, M. Malinowski, R. Mirin, S. Fathpour, Photon pair generation on a silicon chip using nanophotonic periodically-poled lithium niobate waveguides, in: 2018 Conference on Lasers and Electro-Optics (CLEO), (May **2018**), pp. 1–2.
[113] B. S. Elkus, K. Abdelsalam, A. Rao, V. Velev, S. Fathpour, P. Kumar, G. S. Kanter, *Opt. Express* **2019**, *27*, 38521.
[114] J. yang Chen, Y. M. Sua, Z. hui Ma, C. Tang, Z. Li, Y. ping Huang, *OSA Continuum* **2019**, *2*, 2914.
[115] J. Zhao, C. Ma, M. Rüsing, S. Mookherjea, *Phys. Rev. Lett.* **2020**, *124*, 163603.
[116] A. Rao, N. Nader, T. Gerrits, M. J. Stevens, O. S. Magaña-Loaiza, G. F. Camacho-González, J. Chiles, A. Honardoost, M. Malinowski, R. Mirin, S. Fathpour, Spectral resolution of second-order coherence of broadband biphotons, in: 2018 Conference on Lasers and Electro-Optics (CLEO), (May **2018**), pp. 1–2.
[117] J. Leuthold, C. Koos, W. Freude, *Nat. Photonics* **2010**, *4*, 535.
[118] K. Liu, C. R. Ye, S. Khan, V. J. Sorger, *Laser Photonics Rev.* **2015**, *9*, 172.
[119] W. Heni, Y. Kutuvantavida, C. Haffner, H. Zwickel, C. Kieninger, S. Wolf, M. Lauermann, Y. Fedoryshyn, A. F. Tillack, L. E. Johnson, D. L. Elder, B. H. Robinson, W. Freude, C. Koos, J. Leuthold, L. R. Dalton, *ACS photonics* **2017**, *4*, 1576.
[120] A. Rao, S. Fathpour, *IEEE J. Sel. Top. Quantum Electron.* **2018**, *24*, 1.
[121] S. Fathpour, *IEEE J. Quantum Electron.* **2018**, *54*, 1.
[122] P. Rabiei, W. H. Steier, *Appl. Phys. Lett.* **2005**, *86*, 161115.
[123] M. Uddin, H. Chan, *J. Mater. Sci.: Mater. Electron.* **2009**, *20*, 277.
[124] A. Honardoost, G. F. C. Gonzalez, S. Khan, M. Malinowski, A. Rao, J. Tremblay, A. Yadav, K. Richardson, M. C. Wu, S. Fathpour, *IEEE Photonics J.* **2018**, *10*, 1.

[125] S. Fathpour, A. Honardoost, S. Khan November 1 **2018**, US Patent App. 15/932,800.
[126] I. Bakish, R. Califa, T. Ilovitsh, V. Artel, G. Winzer, K. Voigt, L. Zimmermann, E. Shekel, C. N. Sukenik, A. Zadok, Voltage-induced phase shift in a hybrid linbo3-on-silicon mach-zehnder interferometer, in: Advanced Photonics 2013, (Optical Society of America, **2013**), p. IW4A.2.
[127] J. Chiles, S. Fathpour, *Optica* **2014**, *1*, 350.
[128] A. Honardoost, F. A. Juneghani, R. Safian, S. Fathpour, *Opt. Express* **2019**, *27*, 6495.
[129] M. L. Bortz, M. M. Fejer, *Opt. Lett.* **1991**, *16*, 1844.
[130] L. Chen, R. M. Reano, *Opt. Express* **2012**, *20*, 4032.
[131] T. Nagatsuma, G. Ducournau, C. C. Renaud, *Nat. Photonics* **2016**, *10*, 371.
[132] D. A. B. Miller, *Appl. Opt.* **2010**, *49*, F59.
[133] M. Yu, C. Wang, M. Zhang, M. Lončar, *IEEE Photonics Technol. Lett.* **2019**, *31*, 1894.
[134] D. Pohl, M. R. Escalé, M. Madi, F. Kaufmann, P. Brotzer, A. Sergeyev, B. Guldimann, P. Giaccari, E. Alberti, U. Meier et al., *Nat. Photonics* **2020**, *14*, 24.
[135] A. Shams-Ansari, M. Yu, Z. Chen, C. Reimer, M. Zhang, N. Picqué, M. Lončar, *arXiv preprint arXiv:2003.04533* (**2020**).
[136] D. Shrekenhamer, C. M. Watts, W. J. Padilla, *Opt. Express* **2013**, *21*, 12507.
[137] Y. Shen, N. C. Harris, S. Skirlo, M. Prabhu, T. Baehr-Jones, M. Hochberg, X. Sun, S. Zhao, H. Larochelle, D. Englund, M. Soljacic, *Nat. Photonics* **2017**, *11*, 441.
[138] J. L. O'Brien, *Science* **2007**, *318*, 1567.
[139] K. K. Mehta, G. N. West, R. J. Ram, Sin-on-linbo3 integrated optical modulation at visible wavelengths, in: 2017 Conference on Lasers and Electro-Optics (CLEO), (May **2017**), pp. 1–2.
[140] B. Desiatov, A. Shams-Ansari, M. Zhang, C. Wang, M. Lončar, *Optica* **2019**, *6*, 380.
[141] A. Honardoost, R. Safian, A. Rao, S. Fathpour, *J. Lightwave Technol.* **2018**, *36*, 5893.
[142] M. Jin, J. Y. Chen, Y. M. Sua, Y. P. Huang, *Opt. Lett.* **2019**, *44*, 1265.
[143] A. Karim, J. Devenport, *IEEE Photonics Technol. Lett.* **2007**, *19*, 312.
[144] A. Boes, L. Chang, M. Knoerzer, T. G. Nguyen, J. D. Peters, J. E. Bowers, A. Mitchell, *Opt. Express* **2019**, *27*, 23919.
[145] J. T. Nagy, R. M. Reano, *Opt. Mater. Express* **2019**, *9*, 3146.
[146] J. Zhao, M. Rüsing, S. Mookherjea, *Opt. Express* **2019**, *27*, 12025.
[147] M. Rüsing, J. Zhao, S. Mookherjea, *J. Appl. Phys.* **2019**, *126*, 114105.
[148] Y. Niu, C. Lin, X. Liu, Y. Chen, X. Hu, Y. Zhang, X. Cai, Y. X. Gong, Z. Xie, S. Zhu, *Appl. Phys. Lett.* **2020**, *116*, 101104.
[149] J. Zhao, M. Rüsing, M. Roeper, L. M. Eng, S. Mookherjea, *J. Appl. Phys.* **2020**, *127*, 193104.
[150] L. E. Myers, R. C. Eckardt, M. M. Fejer, R. L. Byer, W. R. Bosenberg, J. W. Pierce, *J. Opt. Soc. Am. B* **1995**, *12*, 2102.
[151] A. Rao, S. Fathpour, *Phys. Status Solidi A* **2018**, *215*, 1700684.
[152] A. Rao, J. Chiles, S. Khan, S. Toroghi, M. Malinowski, G. F. Camacho-González, S. Fathpour, *Appl. Phys. Lett.* **2017**, *110*, 111109.
[153] C. Wang, X. Xiong, N. Andrade, V. Venkataraman, X. F. Ren, G. C. Guo, M. Lončar, *Opt. Express* **2017**, *25*, 6963.
[154] A. Rao, T. Sjaardema, G. F. Camacho-González, A. Honardoost, M. Malinowski, K. Schepler, S. Fathpour, Random quasi-phase-matching on a nanophotonic heterogeneous silicon chip, in: Conference on Lasers and Electro-Optics, (Optical Society of America, **2018**), p. SM1B.2.
[155] L. Cai, Y. Wang, H. Hu, *Opt. Commun.* **2017**, *387*, 405.
[156] R. Wolf, I. Breunig, H. Zappe, K. Buse, *Opt. Express* **2017**, *25*, 29927.
[157] R. Luo, H. Jiang, S. Rogers, H. Liang, Y. He, Q. Lin, *Opt. Express* **2017**, *25*, 24531.
[158] R. Luo, Y. He, H. Liang, M. Li, Q. Lin, *Laser Photonics Rev.* **2019**, *13*, 1800288.
[159] R. Luo, Y. He, H. Liang, M. Li, Q. Lin, *Optica* **2018**, *5*, 1006.
[160] D. D. Hickstein, D. R. Carlson, A. Kowligy, M. Kirchner, S. R. Domingue, N. Nader, H. Timmers, A. Lind, G. G. Ycas, M. M. Murnane, H. C. Kapteyn, S. B. Papp, S. A. Diddams, *Optica* **2017**, *4*, 1538.
[161] L. Wang, S. Liu, Y. Kong, S. Chen, Z. Huang, L. Wu, R. Rupp, J. Xu, *Opt. Lett.* **2010**, *35*, 883.
[162] D. Zheng, Y. Kong, S. Liu, M. Chen, S. Chen, L. Zhang, R. Rupp, J. Xu, *Sci. Rep.* **2016**, *6*, 20308.
[163] D. A. Bryan, R. Gerson, H. E. Tomaschke, *Appl. Phys. Lett.* **1984**, *44*, 847.
[164] R. Luo, Y. He, H. Liang, M. Li, J. Ling, Q. Lin, *Phys. Rev. Appl.* **2019**, *11*, 034026.
[165] G. Li, Y. Chen, H. Jiang, X. Chen, *Opt. Lett.* **2017**, *42*, 939.
[166] X. Ye, S. Liu, Y. Chen, Y. Zheng, X. Chen, *Opt. Lett.* **2020**, *45*, 523.
[167] S. Liu, Y. Zheng, Z. Fang, X. Ye, Y. Cheng, X. Chen, *Opt. Lett.* **2019**, *44*, 1456.
[168] T. Sjaardema, M. Malinowski, A. Rao, S. Fathpour, Under preparation for Optica (**2020**).
[169] T. Sjaardema, A. Rao, S. Fathpour, Third- and fourth-harmonic generation in cascaded periodically-poled lithium niobate ultracompact waveguides on silicon, in: Conference on Lasers and Electro-Optics, (Optical Society of America, **2019**), p. STh1J.1.
[170] J. Lin, N. Yao, Z. Hao, J. Zhang, W. Mao, M. Wang, W. Chu, R. Wu, Z. Fang, L. Qiao, W. Fang, F. Bo, Y. Cheng, *Phys. Rev. Lett.* **2019**, *122*, 173903.
[171] S. Liu, Y. Zheng, X. Chen, *Opt. Lett.* **2017**, *42*, 3626.
[172] M. Li, H. Liang, R. Luo, Y. He, Q. Lin, *Laser Photonics Rev.* **2019**, *13*, 1800228.
[173] Y. He, Q. F. Yang, J. Ling, R. Luo, H. Liang, M. Li, B. Shen, H. Wang, K. Vahala, Q. Lin, *Optica* **2019**, *6*, 1138.
[174] Z. Gong, X. Liu, Y. Xu, M. Xu, J. B. Surya, J. Lu, A. Bruch, C. Zou, H. X. Tang, *Opt. Lett.* **2019**, *44*, 3182.
[175] W. Fan, Z. Lu, W. Li, X. Wang, M. Zhou, W. Wang, Q. Sun, G. Wang, D. Cheng, L. Wang, W. Zhang, W. Zhao, *IEEE Photonics J.* **2019**, *11*, 1.
[176] B. Buscaino, M. Zhang, M. Lončar, J. M. Kahn, *J. Lightwave Technol.* **2020**, *38*, 1400.
[177] G. F. C. Gonzalez, M. Malinowski, A. Honardoost, S. Fathpour, *Appl. Opt.* **2019**, *58*, D1.
[178] Y. Okawachi, M. Yu, B. Desiatov, B. Y. Kim, T. Hansson, M. Lončar, A. L. Gaeta, *arXiv preprint arXiv:2003.11599* (**2020**).
[179] K. Abdelsalam, T. Li, J. B. Khurgin, S. Fathpour, *Optica* **2020**, *7*, 209.
[180] N. Gisin, G. Ribordy, W. Tittel, H. Zbinden, *Rev. Mod. Phys.* **2002**, *74*, 145.
[181] F. Lenzini, J. Janousek, O. Thearle, M. Villa, B. Haylock, S. Kasture, L. Cui, H. P. Phan, D. V. Dao, H. Yonezawa, P. K. Lam, E. H. Huntington, M. Lobino, *Sci. Adv.* **2018**, 4.
[182] H. Jin, F. M. Liu, P. Xu, J. L. Xia, M. L. Zhong, Y. Yuan, J. W. Zhou, Y. X. Gong, W. Wang, S. N. Zhu, *Phys. Rev. Lett.* **2014**, *113*, 103601.
[183] O. Alibart, V. D'Auria, M. De Micheli, F. Doutre, F. Kaiser, L. Labonté, T. Lunghi, É. Picholle, S. Tanzilli, *J. Opt.* **2016**, *18*, 104001.
[184] K. H. Luo, S. Brauner, C. Eigner, P. R. Sharapova, R. Ricken, T. Meier, H. Herrmann, C. Silberhorn, *Sci. Adv.* **2019**, *5*, eaat1451.

Amirmahdi Honardoost received his B.Sc. degree in electrical engineering from Shahid Beheshti University, Tehran, Iran, in 2012, and his M.Sc., and Ph.D. degrees in electrical engineering from the University of Central Florida (UCF), Orlando, FL, in 2016, and 2020, respectively. He is currently working as a postdoctoral scholar in the Electrical Engineering and Computer Sciences Department at University of California, Berkeley. His research interests include photonic integrated circuits focusing on thin-film lithium niobate devices.

Kamal Abdelsalam received his B.Sc. (Distinction with Honors) and M.Sc. degrees in electrical engineering from Ain Shams University, Cairo, Egypt and M.Sc. degree in optics and photonics from UCF. Currently, He is pursuing his Ph.D. in optics and photonics at CREOL, focusing on design, fabrication and characterization of photonic integrated circuits on heterogeneous integrated photonics platforms for quantum- and nonlinear-optic applications.

Sasan Fathpour is a professor of optics and photonics at CREOL. He also holds a joint appointment with the Department of Electrical and Computer Engineering, UCF. He received his Ph.D. degree in electrical engineering from the University of Michigan, Ann Arbor, in 2005. Before joining the CREOL faculty in 2008, he was with the Electrical Engineering Department of UCLA, as a post-doctoral fellow. His current research interests include heterogeneous integrated photonics, nonlinear integrated optics, silicon photonics, and unconventional optical waveguide platforms for mid-wave infrared and other applications.